Title: Hyperinsulinemia acts through acinar cell insulin receptors to drive obesity-associated pancreatic cancer initiation by promoting digestive enzyme production and inflammation

Authors: Anni M.Y. Zhang[1], Yi Han Xia[1], Jeffrey S.H. Lin[1], Ken H. Chu[1], Titine J.J. Ruiter[1], Jenny C.C. Yang[1], Nan Chen[1], Justin Chhuor[1], Shilpa Patil[1], Haoning Howard Cen[1], Elizabeth J. Rideout[1], Vincent R. Richard[3], David F. Schaeffer[2], Rene P. Zahedi[3,4,5], Christoph H. Borchers[3,6], James D. Johnson[1]*, Janel L. Kopp[1]*

Affiliations: [1]Department of Cellular and Physiological Sciences, Life Sciences Institute, University of British Columbia, Vancouver, Canada; [2]Department of Pathology and Laboratory Medicine, University of British Columbia, Vancouver, Canada; [3]Segal Cancer Proteomics Centre, Lady Davis Institute, Jewish General Hospital, McGill University, Montreal, Canada. [4]Department of Internal Medicine, University of Manitoba, Winnipeg, Canada. [5]Manitoba Centre for Proteomics and Systems Biology, Winnipeg, Canada. [6]Gerald Bronfman Department of Oncology, Jewish General Hospital, McGill University, Montreal, Canada.

***Correspondence**: janel.kopp@ubc.ca or james.d.johnson@ubc.ca

Keywords: pancreatic ductal adenocarcinoma, PanIN, hyperinsulinemia, obesity, insulin resistance

Funding: The project was supported by CIHR grants to E.J.R (PJT-153072), J.L.K. (MOP-142216 and PJT-162239) and J.D.J. (PJT - 168854) and by a Lustgarten Foundation Therapeutics Focused Research Program grant to J.D.J. and J.L.K. A.M.Y.Z was supported by Frederick Banting and Charles Best Canada Graduate Scholarships and a Four-Year Fellowship from the University of British Columbia. J.L.K was supported by a CIHR New Investigator Award (Msh-147794) and the MSFHR Scholar Award (18309). E.J.R was supported by the CIHR Sex and Gender Chair Program (GSA-171465) and the MSFHR Scholar Award (16876). C.H.B is grateful to Genome Canada for financial support through the Genomics Technology Platform (GTP: 264PRO) and the Quebec Cancer Consortium, Ministère de l'Économie et de l'Innovation, Quebec. C.H.B is also grateful for support from the Segal McGill Chair in Molecular Oncology at McGill University (Montreal, Quebec, Canada),

and for support from the Warren Y. Soper Charitable Trust and the Alvin Segal Family Foundation to the Jewish General Hospital (Montreal, Quebec, Canada).

Author Contributions: A.M.Y.Z designed, managed, and conducted the project including acquiring and interpreting the majority of the data and she wrote the manuscript. Y.X performed the proteomics and phospho-proteomics analyses. K.H.C and J.C provided technical assistance with pancreas sectioning and staining (Alcian blue, H&E, Ck19, or GFP). J.S.H.L and T.J.J.R provided technical assistance with dissection and genotyping and J.S.H.L performed the explant experiments. J.C.C.Y provided technical assistance with dissection and Ck19 staining. N.C analysed staining (Sirius Red). S.P assisted on dissection and sample preparation. H.H.C assisted with proteomics sample preparation and proteomics analyses. E.J.R evaluated the manuscript and helped with interpretation of the data in a sex-specific manner. V.R.R, R.P.Z and C.H.B co-designed and conducted proteomic analyses. D.F.S provided histopathology analysis and expertise. C.H.B, J.L.K, and J.D.J supervised the project, obtained funding, interpreted the data, and edited the manuscript. J.L.K is the guarantor of this work.

Acknowledgements: The authors thank members from Johnson and Kopp labs for discussions. We thank Christopher Wright (Vanderbilt, USA) for the *Ptf1a*^{CreER} mice.

Conflict of interest: The authors report no relevant conflicts of interest.

Availability of data and materials: All data generated and analyzed in this study is included within the article, additional files, or is available from the corresponding author on request.

Abstract

The rising incidence of pancreatic cancer is largely driven by the skyrocketing prevalence of obesity and type 2 diabetes (T2D). Hyperinsulinemia is a cardinal feature of both conditions, and is independently associated with increased cancer incidence and mortality. Our previous studies demonstrated that genetically reducing insulin production suppressed formation of pancreatic intraepithelial neoplasia (PanIN) pre-cancerous lesions in mice with mutant *Kras*. However, we found that hyperinsulinemia affected many cell types in the pancreatic microenvironment. Thus, it remained unclear whether hyperinsulinemia exerted its effects directly on the cells that give rise to PanINs or indirectly on the tumor microenvironment, and molecular mechanisms involved were unknown. Here, we tested whether insulin receptors (*Insr*) in *Kras*^{G12D}-expressing pancreatic acinar cells are necessary for the effects of hyperinsulinemia on obesity-associated pancreatic cancer development. Loss of *Insr* in Kras^{G12D}-expressing acinar cells did not prevent hyperinsulinemia or weight gain associated with high fat diet (HFD) consumption in mice. However, solely reducing *Insr* in Kras^{G12D}-expressing acinar cells significantly reduced formation of PanIN and tumors, in a gene dose-dependent manner. Mechanistically, proteomic analyses showed that hyperinsulinemia acts through *Insr* to drive the excess production of digestive enzymes in acinar cells by modulating the activity of the spliceosome, ribosome, and secretory machinery. This resulted in increased inflammation, which was abrogated by acinar-specific *Insr* knockout. We confirmed that insulin increased the conversion of wild-type acinar cells into acinar-to-ductal metaplasia (ADM) in a trypsin-dependent manner. Collectively, these data demonstrate that hyperinsulinemia acting via acinar cells insulin receptors promotes inflammatory conditions that cooperate with Kras signaling to increase the risk of developing pancreatic cancer, mechanistically linking obesity and pancreatic cancer.

Introduction

The 5-year survival rate of pancreatic ductal adenocarcinoma (PDAC) is less than 10% and it is projected to become the 2nd leading cause of cancer death by 2030 (Rahib et al., 2014). Chronic pancreatitis, family history, smoking, obesity, and T2D are risk factors for pancreatic cancer (Ilic and

Ilic, 2016). Obesity and T2D are usually accompanied by hyperinsulinemia, hyperglycemia, increased inflammation, and dyslipidemia, which have all been proposed as underlying factors that drive the increased PDAC morbidity and mortality in this patient population (Gallagher and LeRoith, 2020; Zhang et al., 2021). Epidemiological studies consistently show that hyperinsulinemia is associated with increased risk of developing PDAC and poorer survival (Pisani, 2008; Stolzenberg-Solomon et al., 2005). Complementing clinical observations, our *in vivo* animal experiments demonstrated that endogenous hyperinsulinemia causally contributes to PDAC development, independently of hyperglycemia (Zhang et al., 2022; Zhang et al., 2019). Single-cell analysis revealed that hyperinsulinemia altered gene expression in multiple cell types in the PanIN microenvironment (Zhang et al., 2022), leaving open the question of whether the protective effects of reduced insulin production are direct on the tumor precursor cells or whether they are mediated indirectly by local immune cells, local fibroblasts, and/or via distant effects on adiposity (Mehran et al., 2012; Templeman et al., 2015; Templeman et al., 2017). Consistent with a direct effect on the epithelium, insulin stimulates proliferation in the PANC-1 and HPDE cell lines *in vitro* (Chan et al., 2014a), but this does not provide information on the initiation of PDAC *in vivo*.

Insulin/IGF signaling, which includes KRAS/MAPK/ERK or PI3K/AKT/mTOR cascades, is prominent in human and animal pancreatic cancer. Activating mutations in *KRAS* are detected in ~95% of PDAC clinical cases and induce PanIN pre-cancerous lesions and rare tumours in mice (Waters and Der, 2018). Activating mutations in *PIK3CA* are also found in 3-5% of PDAC patients (Heestand and Kurzrock, 2015; Janku et al., 2013) and can initiate PDAC in mice (Payne et al., 2015). Additionally, *Pik3ca* silencing was protective in *Pdx1*-Cre;*Kras*$^{LSL\text{-}G12D}$;*Trp53*$^{LSL\text{-}R172H}$ mice (Sivaram et al., 2019). Strategies that systemically reduce signaling downstream of Insr/Igf1r can suppress PDAC (Hopkins et al., 2018; Payne et al., 2015), but they do not distinguish between the roles for insulin, IGFs, or other upstream growth factors. Despite indirect evidence for an important role of insulin/IGF signaling in this and other cancers, a direct and causal role for the insulin receptor alone has not been demonstrated for any cancer. Insulin receptor protein is increased in some breast, prostate, and liver

cancers (Aljada et al., 2015; Belfiore et al., 2017; Law et al., 2008), but its role in the pancreas remains enigmatic.

In this study, we tested the hypothesis that hyperinsulinemia-induced enhancement of PDAC initiation is mediated through direct insulin receptor signaling in pancreatic acinar cells. We found mice that consumed a high fat diet had a significant reduction in PanIN and tumor development when they lacked *Insr* specifically in $Kras^{G12D}$-expressing acinar cells. These findings indicate that hyperinsulinemia directly contributes to pancreatic cancer initiation through Insr in acinar cells via a mechanism that involves increased production of digestive enzymes and subsequent pancreatic inflammation.

Results

Effects of acinar cell-specific *Insr* loss on body weight and glucose homeostasis

We first generated *Ptf1a*^{CreER};*Insr*$^{w/w}$;nTnG or *Ptf1a*^{CreER};*Insr*$^{f/f}$;nTnG mice to assess the baseline roles of *Insr* in acinar cells (Figure 1A). All mice were fed with HFD after 3 weeks of age to sustain hyperinsulinemia. Tamoxifen was injected at 4 weeks of age to induce recombination of the *Insr*^{flox} alleles and a Cre-dependent nTnG allele (Muzumdar et al., 2007), specifically in acinar cells (Figure 1B). As expected, mice consuming HFD gained weight over time. We did not find a significant difference in body weight between male *Ptf1a*^{CreER};*Insr*$^{f/f}$;nTnG mice and *Ptf1a*^{CreER};*Insr*$^{w/w}$;nTnG mice but observed a significant and consistent reduction in body weight in female *Ptf1a*^{CreER};*Insr*$^{f/f}$;nTnG mice compared to *Ptf1a*^{CreER};*Insr*$^{w/w}$;nTnG mice (Figures 1C-D), perhaps as a result of a minor pancreatic insufficiency (see below). Fasting glucose was not different between genotypes (Figures 1E-F). HFD induced similar levels of hyperinsulinemia in both genotypes (Figures 1G-H) and males, as previously reported (Zhang et al., 2022; Zhang et al., 2019), had higher overall levels of insulin compared to females on HFD (Figures 1G-H). These insulin levels are well above the expected fasting insulin levels of C57Bl6J mice on a chow diet (138 +/- 24 pM) (Berglund et al., 2008) and higher than we have previously reported in mice with reduced insulin gene dosage (Zhang et al., 2022; Zhang et al., 2019). Pancreas weight of *Ptf1a*^{CreER};*Insr*$^{w/w}$;nTnG and *Ptf1a*^{CreER};*Insr*$^{f/f}$;nTnG mice were not

different at 12 weeks of age (Figure 1I). These data demonstrate that mice with acinar-specific *Insr* deletion having wild type-like pancreata.

Body weight and glucose homeostasis in mice with acinar-specific *Insr* loss and Kras mutation

To test our primary hypothesis, that hyperinsulinemia drives pancreatic cancer development via Insr cell autonomously, we generated mouse models in which *Kras*^{G12D} expression (Kopp et al., 2012) and loss of *Insr* were both induced in acinar cells. Our cohorts contained mice with full *Insr* gene dosage, *Ptf1a*^{CreER};*Kras*$^{LSL\text{-}G12D}$;*Insr*$^{w/w}$;nTnG (PK-*Insr*$^{w/w}$); mice with reduced *Insr* , *Ptf1a*^{CreER};*Kras*$^{LSL\text{-}G12D}$;*Insr*$^{w/f}$;nTnG (PK-*Insr*$^{w/f}$); or mice without *Insr*, *Ptf1a*^{CreER};*Kras*$^{LSL\text{-}G12D}$;*Insr*$^{f/f}$;nTnG (PK-*Insr*$^{f/f}$) in Kras^{G12D}-expressing acinar cells (Figure 2A). In this model, tamoxifen induced simultaneous acinar-specific recombination to express mutant *Kras*^{G12D}, a nTnG, and deletion of *Insr*^{flox} alleles. Multiple studies have shown that HFD accelerates PanIN and PDAC development (Chang et al., 2017; Dawson et al., 2013). *Insr* loss in acinar cells did not significantly affect the weight gain of male or female mice in the context of mutant *Kras* (Figures 2B-C). Fasting glucose and insulin levels were also similar between groups (Figures 2D-G). Thus, our model enabled us to test the role of acinar cell *Insr* in the context of intact hyperinsulinemia and normoglycemia, which normally occurs in the obese state.

Loss of *Insr* in *Kras*^{G12D}-expressing acinar cells reduced PanIN development

To test whether *Insr* loss affected Kras^{G12D}-mediated PDAC formation from acinar cells, we examined a cohort of 9-12 PK-*Insr*$^{w/w}$, PK-*Insr*$^{w/f}$, and PK-*Insr*$^{f/f}$ mice for each sex and genotype and planned to assess lesions at ~1 year of age based on our previous work (Zhang et al., 2022; Zhang et al., 2019). However, half the male PK-*Insr*$^{w/w}$ mice and a few female PK-*Insr*$^{w/w}$ mice reached humane endpoint earlier than we had expected (Figure 3A). This suggested that HFD promoted tumor development in mice with full insulin gene dosage earlier than in mice with reduced insulin (Zhang et al., 2022; Zhang et al., 2019). Through necropsy we noted that macroscopic tumors were present in male PK-*Insr*$^{w/w}$ mice reaching humane endpoint (Figure 3A). Additionally, the remaining male PK-

167 *Insr*$^{w/w}$ mice had PDAC or the parenchyma was almost completely replaced by ductal metaplasia
168 comprising cysts, PanIN, and ADM at 43.5 weeks of age (Figure 3A-B). Three male PK-*Insr*$^{w/f}$ mice
169 also reached human endpoint prior to 43.5 weeks, but tumors were not observed at necropsy (Figure
170 3A). Finally, no male PK-*Insr*$^{f/f}$ mice reached humane endpoint by 43.5 weeks of age (Figure 3A).
171 PDAC was noted by histology in 40-50% of PK-*Insr*$^{w/f}$ mice and PK-*Insr*$^{f/f}$ mice (Figures 3A-C). In sum,
172 male PK-*Insr*$^{f/f}$ mice lived longer than PK-*Insr*$^{w/f}$ mice and PK-*Insr*$^{w/w}$ mice and had more normal
173 parenchyma left at 40.5 weeks of age suggesting that loss of *Insr* in Kras^{G12D}-expressing acinar cells
174 limits HFD-mediated promotion of acinar cell transformation.

175 As noted above, a few female PK-*Insr*$^{w/w}$ mice, as well as a few PK-*Insr*$^{w/f}$ mice also reached
176 humane endpoint prior to 43.5 weeks, but no macroscopic tumors were noted at necropsy (Figure 3A).
177 No female PK-*Insr*$^{f/f}$ mice reached humane endpoint by 43.5 weeks of age. Histologically, we found
178 that the incidence of PDAC in females was *Insr* dosage-dependent (Figures 3A-C). The majority of
179 female mice from every genotype, retained some normal parenchyma (Figures 3B-C). This suggested
180 that the extent of disease in females at 10 months of age was different than males and that female
181 mice had not yet maximally disrupted normal parenchyma function. This is consistent with previous
182 reports suggesting that the timing and/or extent of lesion formation between male and female mice in
183 the context of HFD may differ (Chang et al., 2017). Altogether, these data strongly suggested that
184 limiting or eliminating insulin/Insr activity specifically in acinar cells in male and female mice reduced
185 the propensity of HFD and Kras activation to transform the pancreas.

186 We next quantified the extent of the tissue disruption and lesion formation at 43.5 weeks of age to
187 assess the extent of disease present in the presence or absence of *Insr*. In parallel with PanIN
188 quantification between groups, we stained for nuclear GFP from the nTnG lineage reporter allele
189 (Muzumdar et al., 2007) in all pancreata. As expected, most acinar cells and PanIN lesions were GFP
190 positive (Figures S1A-B) confirming that the lesions arose from Ptf1a^{+} acinar cells. Rare mice with a
191 GFP labeling efficiency of acinar cells below 20% were excluded from further analysis. Pancreata from
192 *Ptf1a*^{CreER};*Insr*$^{w/w}$;nTnG and *Ptf1a*^{CreER};*Insr*$^{f/f}$;nTnG mice were similarly comprised of acinar cells and
193 endocrine islets and by IHC had GFP expression widely present in acinar cells (Figures S1C-F),

194 consistent with their *Kras* wild-type genotype. In contrast, pancreata from male and female PK-*Insr*$^{w/w}$,
195 PK-*Insr*$^{w/f}$, and PK-*Insr*$^{f/f}$ mice all contained ductal lesions with histological characteristics of
196 metaplastic ducts, including ADM, low-grade and high-grade PanIN, and sometimes PDAC (see
197 above) (Figures 3B-C). When we quantified the PanIN and/or tumor area, we found that reducing *Insr*
198 in Kras^{G12D}-expressing acinar cells reduced the area of PanINs plus tumors, PanIN alone, or tumor
199 area in a dose dependent manner in males and females (Figures 3D-F). Consistent with this
200 histological-based quantification, measuring the pancreatic area containing ductal metaplasia (ducts,
201 ADM, PanIN and PDAC) or mucinous lesions (PanIN and some tumors) with Ck19 or Alcian blue
202 staining, respectively, similarly showed that female PK-*Insr*$^{w/w}$ mice formed significantly more lesions
203 than female PK-*Insr*$^{f/f}$ mice (Figures S2A-D). Notably, male PK-*Insr*$^{w/w}$ mice had a higher Ck19^{+}, but a
204 similar amount of Alcian blue^{+} area compared to other genotypes. This latter observation is likely
205 explained by the presence of Alcian blue negative high-grade PanIN lesions and large cysts with
206 predominantly normal ductal epithelium which were more prevalent in male than female, PK-*Insr*$^{w/w}$
207 pancreata (Figure 3B and Figures S2A, S2C, S2E-F). Indeed, most male PK-*Insr*$^{w/w}$ and some female
208 PK-*Insr*$^{w/w}$ pancreata were comprised of almost all Ck19^{+} area with little acinar cell area left, while
209 larger areas of normal acinar cells correlated with lower Ck19^{+} areas in PK-*Insr*$^{w/f}$ and PK-*Insr*$^{f/f}$ mice
210 (Figures 3B-C, Figure 3G and Figures S2G-H). Therefore, our data strongly suggested that acinar cell
211 *Insr* dose-dependently regulates oncogenic Kras-induced PanIN initiation in the context of diet-
212 induced hyperinsulinemia.
213
214 **Loss of *Insr* in *Kras*^{G12D}-expressing acinar cells reduced PanIN initiation**
215 To examine whether PanIN initiation was specifically affected by loss of *Insr* in acinar cells, we
216 examined 12-week-old male and female mice of each genotype. At 8 weeks post-tamoxifen injection,
217 acinar cells and PanIN lesions were also GFP positive indicating good recombination efficiency
218 (Figures S3A-B). There were no significant differences in pancreas weight between PK-*Insr*$^{w/w}$, PK-
219 *Insr*$^{w/f}$, and PK-*Insr*$^{f/f}$ mice in either sex (Figure 4A). This is consistent with previous data showing that
220 the pancreas was largely normal in young *Ptf1a*^{CreER};*Kras*$^{LSL-G12D}$ mice (Kopp et al., 2012). Pancreata

from PK-*Insr*$^{f/f}$ mice were predominantly normal with a small number of ductal lesions having characteristics of ADM or low-grade PanIN (Figures 4B-D). In contrast, significantly more of the pancreas was occupied by PanIN in PK-*Insr*$^{w/w}$ mice (Figures 4B-D). The significant inhibition of PanIN formation solely through reducing *Insr* in acinar cells strongly supports a model in which the primary mechanism by which diet-induced hyperinsulinemia promotes tumor initiation is through insulin receptors on acinar cells.

Proteomic and phospho-proteomic analyses of pancreata from mice lacking acinar *Insr*

To investigate the underlying molecular mechanisms of *Insr* action in PanIN initiation, we conducted unbiased total and phospho-proteomic analyses using the head of the pancreas from the 12-week-old female mice (Figure 4) with and without Kras^{G12D} and/or *Insr*. For the total proteome dataset, we obtained reliable, quantitative data on 2889 proteins across all the samples. Consistent with our histological analyses identifying a change in PanIN, we found that the inflammation- and PanIN-associated proteins, Reg3a, Reg3b, Reg2, Tff1, Gkn1, and Gkn2 (Chen et al., 2019; Li et al., 2016; Steiner et al., 2022), were among the 124 proteins significantly enriched in PK-*Insr*$^{w/w}$ compared to *Ptf1a*^{CreER};*Insr*$^{w/w}$;nTnG pancreata (Figure 5A and Table S1). We also found that some proteins associated with acinar cell function, such as Ctrc, Dbi, Pla2g1b, and Clps, were among the 122 proteins significantly down-regulated as a consequence of *Kras*^{G12D} expression in acinar cells (Figure 5A). However, the majority of proteins associated with acinar cell function, like Cpa1, Spink1, and Cela1, remain unchanged between the PK-*Insr*$^{w/w}$ and *Ptf1a*^{CreER};*Insr*$^{w/w}$;nTnG genotypes (Table S1). Importantly, we compared the differentially expressed pathways between PK-*Insr*$^{w/w}$ and *Ptf1a*^{CreER};*Insr*$^{w/w}$;nTnG mice to differentially expressed pathways between human PDAC and normal pancreas tissues adjacent to human PDAC (Cao et al., 2021) (Figures S4A-B). We found that most of the pathways were significantly enriched in both mouse and human datasets, which suggested our proteomic and phospho-proteomic results were relevant to human samples. Interestingly, we also found 92 proteins increased in abundance and 155 proteins had decreased abundance solely due to loss of *Insr* in Kras wild-type acinar cells (Figure 5B), with the caveat that we analyzed a low sample

number. Nevertheless, reductions in Ctrc, Clps, Pla2g1b suggested that *Insr* may have a role in regulating the function of wild-type acinar cells in mice fed HFD (Figure 5C).

To define the molecular mechanisms associated with *Insr* deletion in the context of mutant Kras, we focused further analyses on comparing the PK-*Insr*$^{f/f}$ pancreata to the PK-*Insr*$^{w/w}$ pancreata. We found that 135 proteins were enriched and 117 were depleted in PK-*Insr*$^{f/f}$ mice compared to PK-*Insr*$^{w/w}$ controls (Figure 5C). We then used these differentially expressed genes to perform a K-means clustering analysis with the differentially abundant genes between PK-*Insr*$^{w/w}$ and PK-*Insr*$^{f/f}$ mice using the protein abundance values in all genotypes to groups of proteins that varied by Insr status, Kras mutation, or both (Figure 5D). As expected from our histological analyses, proteins associated with PanIN initiation or formation in PK-*Insr*$^{w/w}$ compared to *Ptf1a*^{CreER};*Insr*$^{w/w}$;nTnG pancreata, such as Reg3a, Reg3b, Reg2, Tff1, Gkn1, and Gkn2, (Figure 5A and 5D, cluster 1), were reduced in PK-*Insr*$^{f/f}$ mice (Figure 5C, Figure 5D, cluster 1 and Table S4). In order to investigate potential functional enrichment of protein groups based on cell signaling, intracellular localization, and biological process, we used the differentially abundant proteins between PK-*Insr*$^{w/w}$ and PK-*Insr*$^{f/f}$ mice (Adj. $p<0.05$) to build protein-protein interaction networks using STRING (Szklarczyk et al., 2021) and assigned these proteins to their intracellular organelle locations in a diagram using the COMPARTMENTS section of GeneCards and/or existing knowledge of their function (Binder et al., 2014) (Figure 6A). This data depiction (Figure 5D, cluster 2 and 3) highlighted the striking downregulation of the majority of the proteins packaged into zymogen granules for secretion in PK-*Insr*$^{f/f}$ compared to *Ptf1a*^{CreER};*Insr*$^{w/w}$;nTnG and PK-*Insr*$^{w/w}$ mice (Figure 6A-B). Acinar cells produce a large amount of protein every day, and in *Ptf1a*^{CreER};*Insr*$^{w/w}$;nTnG mice fed HFD, 18.7% of the peptides detected in our analyses were associated with the zymogen granules and this was similar in *PK-Insr*$^{w/w}$ pancreata (18.7%) (Figure 6C). However, this percentage was reduced significantly to 12.2% in PK-*Insr*$^{f/f}$ pancreata, as well as to 16% in *Ptf1a*^{CreER};*Insr*$^{f/f}$;nTnG pancreata (Figure 6C). This reduction in zymogen proteins is likely an underestimate of the effect on the total proteome, as our differential abundance analyses were normalized to total protein content. Thus, loss of *Insr* in acinar cells results

in a coordinated decrease in the amount of digestive enzyme produced by acinar cells in the context of HFD.

Pancreatic acinar cells represent the cellular majority in our bulk tissue proteome. With the caveat that our bulk tissue includes multiple cell types, our STRING network analysis nevertheless highlighted potential mechanisms downstream of *Insr* loss that could underlie this dramatic reduction in zymogen granule content in acinar cells. This included increases in proteins with key roles in suppressing protein synthesis at the ribosome (eEF2K) and suppressing insulin signaling (Ptpn1), as well as increases in the first enzyme of the fatty acid beta oxidation pathway (Acox1), a protein regulating lysosome function (Grn), and protein processing machinery at the ER and Golgi (Ilvbl, Ssr3, Ssr4, Irag2). Many components of mitochondrial electron transport complexes were changed, as well as endosomal and cytoskeletal proteins, many of which are involved in moving organelles within the cells or in exocytosis, such as Snx5, Vps35l, Sycn (Figure 6A). Finally, we also found decreases in critical parts of the spliceosome (Snrpa), the signal recognition particle complex receptor (Srprb), and components of the large ribosome (Rpl29, Rpl36, Rpl37a). Altogether, these observations suggested that loss of *Insr* in acinar cells and a reduction in PanIN formation is associated with a reduction in synthesis of digestive enzymes.

Parallel phosphoproteomic analysis on the same samples confirmed and extended the findings from our total proteomic analysis (Figure 7A-D). We identified 225 downregulated phospho-peptides and 177 upregulated phospho-peptides by comparing the PK-*Insr*$^{f/f}$ pancreas to PK-*Insr*$^{w/w}$ controls (Figure 7A). In general, statistically significant phospho-peptide differences were not due to underlying differences in total protein abundance (Figure 7B). Using a similar strategy as above, we mapped the function of the proteins to compartments and processes in the cell (Figure 7D). We found significant decreases in phosphorylation in PK-*Insr*$^{f/f}$ compared PK-*Insr*$^{w/w}$ pancreata for proteins involved in transcription elongation (Eloa, Top2a, Supt5h), mRNA splicing and nuclear speckle formation (Srpk1, many Srsf proteins, Cherp, Srrm1 and Srrm2), as well as protein translation initiation (Eif4b, Eif5b, and eIF3 complex proteins) and elongation (Eef1b, Eef1d, and many ribosomal subunits). There were also decreases in phospho-peptides for Cavin3, which has been implicated in Akt-Erk signaling bias

(Haoning Howard Cen, 2022; Hernandez et al., 2013), and PP1 inhibitor Ppp1r2, at sites known to be influenced by insulin signaling (Figure 7D). Finally, there was reduced phosphorylation of Larp1 at sites known to be regulated by Raptor and Rictor. Larp1 is an RNA-binding protein that links mTorc1 to the regulation of terminal oligopyrimidine tract (TOP) mRNA that encodes for ribosomal proteins and elongation factors (Hong et al., 2017). Altogether, our proteomics data suggested that Insulin/Insr promotes the production of proteins in acinar cells in part through its modulation of Larp1 and many other components controlling transcription, translation, and secretion of digestive enzymes. Interestingly, multiple sites on the cholecystokinin (Cck) receptor (Cckar) also showed altered phosphorylation (Figure 7C-D), including sites in the main intracellular loop that are indicative of ligand-induced desensitization (Rao et al., 2000) and phospho-sites in the C-terminal tail that have not been previously reported. Collectively, these unbiased total and phospho-proteomic studies delineate the possible molecular mechanisms by which hyperinsulinemia, acting via the Insr, may promote Kras-driven pancreatic cancer initiation.

Our histological analyses, as well as our total proteomics and phosphoproteomics suggested that loss of the *Insr* in acinar cells prevented the formation of PanIN and prevented the induction of genes associated with pancreatic injury, such as Reg3a, Reg3b, and Reg2. To examine whether loss of *Insr* in acinar cells prevented the injury and/or fibrosis typically associated with $Kras^{G12D}$ activation and PanIN formation, we performed Sirius Red staining on 12-week-old pancreata (Figures 8A-B). In PK-$Insr^{w/w}$ control pancreata, Sirius Red staining surrounded the metaplastic ducts, containing ADM and PanIN, as well as the surrounding acini in nearby lobules (Figures 8A-B). In contrast, in the PK-$Insr^{f/f}$ pancreata, the metaplasia that did form tended to be associated with less Sirius Red staining and less staining in the neighboring lobules (Figures 8A-C). In male PK-$Insr^{w/w}$ pancreata, the extent of Sirius Red staining significantly correlated with the amount of PanINs formed (Figure S5A). In female PK-$Insr^{w/w}$ pancreata, there were higher than expected amounts of Sirius Red given the amount of PanIN observed, but the relationship between the values was still strong (Figure S5B). However, in the absence of *Insr* very few PanIN formed in both sexes and this was associated with a lower amount of

Sirius Red staining, especially in females. This supported our hypothesis that inflammation was reduced in the absence of *Insr* in Kras^{G12D}-expressing acinar cells.

Our proteomics data suggested that fewer digestive enzymes were present in the absence of Insr in acinar cells when Kras^{G12D} expression was also present (Figure 6). Given that autoactivation of trypsinogen in acinar cells or in the pancreatic parenchyma contributes, at least in part, to the induction of pancreatitis (Smith and Solomon, 2014), we reasoned that the reduced presence of enzymes in the absence of *Insr* could result in less tissue damage spreading into other lobules. This would result in decreased ADM and PanIN formation, as in the PK-*Insr*$^{f/f}$ pancreata. To test this hypothesis, we utilized an 3D *ex vivo* model of ADM formation from wild-type acinar cells (Figure 8D) (Fleming Martinez and Storz, 2019; Means et al., 2005a). Wild-type acinar clusters grown in collagen for 5 days maintained their acinus morphology, as previously shown (Means et al., 2005a). In addition, treatment with TGF-α induced these clusters to form a duct-like lumen structure (Figure 8E) (Means et al., 2005b). Addition of increasing concentrations of insulin alone had only a modest effect on acini clusters (Figure 8E-F). However, increasing concentrations of insulin in combination with TGF-α induced ring formation significantly (Figure 8E-F). Remarkably, the synergism between insulin and TGF-α was significantly reduced by the presence of trypsin inhibitor in the culture media (Figure 8F). Because acinar cells are the source of trypsinogen and this pro-enzyme is prone to autoactivation, our data suggested that hyperinsulinemia-mediated promotion of enzyme production in acinar cells can result in increased inflammation and promote initiation of PanIN lesions from acinar cells sustaining activating mutations in *Kras* (Figure 8G).

Discussion

The purpose of this study was to test the hypothesis that hyperinsulinemia in the obese state acts directly on acinar cells to promote pancreatic cancer initiation. Our data clearly support a model where Insr in acinar cells plays a causal role in supporting cancer initiation in the context of diet-induced obesity and mutant Kras. The contribution of direct insulin action on acinar cells during initiation from normal cells explains a large portion of the effects of HFD, but our results do not preclude roles for Insr

in other local or distant cell types (Zhang et al., 2022) and at other times during the progression of the initial precursor lesions to PDAC. Our unbiased proteomic and phospho-proteomic analyses led us to propose a model in which HFD and hyperinsulinemia through Insr in acinar cells promote the physiological function of acinar cells to supply digestive enzymes to breakdown lipid rich food in the duodenum. However, the increased presence of enzymes increases the risk of autoactivated trypsin, as well. This increased propensity for trypsin-induced injury would result in sub-clinical levels of inflammation and acinar-to-ductal metaplasia. Thus, the physiological response of pancreas to a diet rich in fat results in increased insulin production from beta cells, which further promotes an increased enzyme production capacity in acinar cells. However, in the context of *Kras* mutations, this increased production can lead to increased chances of inflammation that enhance $Kras^{G12D}$ signaling and promote an irreversible transformation in $Kras^{G12D}$-expressing acinar cells. Thus, our studies provide a key missing link explaining the connection between obesity and hyperinsulinemia and increased pancreatic inflammation and PanIN initiation.

Diet-induced obesity induces insulin hypersecretion, increases beta cell mass and impairs insulin clearance, resulting in sustained hyperinsulinemia (Mehran et al., 2012; Zhang et al., 2021). Mice used in this study, which had the full complement of all 4 insulin alleles (*Ins1* and *Ins2*), exhibited higher fasting insulin levels (males 1000-1500 pmol/L; females 500 pmol/L) than our previous models with insulin gene dosage reduced to 1 or 2 copies (males, 400-800 pmol/L; females 100-200 pmol/L) (Zhang et al., 2022; Zhang et al., 2019). Consistent with our working model that endogenous hyperinsulinemia contributes to pancreatic cancer development, more than 90% of the normal pancreatic area in the PK-$Insr^{w/w}$ mice in this study was replaced by ductal metaplasia, PanIN, and tumors at 10 months of age. Notably, 1-year-old PK-$Ins1^{+/+}$;$Ins2^{-/-}$ control mice had just ~25% of the pancreas replaced by PanINs, while PK-$Ins1^{-/-}$;$Ins2^{+/+}$ mice were at ~1-4% by 1 year of age (Zhang et al., 2022; Zhang et al., 2019). If only considering PDAC, ~70% of female PK-$Insr^{w/w}$ mice developed PDAC in this study at 10 months of age, while only 1 female PK-$Ins1^{+/+}$;$Ins2^{-/-}$ mouse developed PDAC after a year (Zhang et al., 2022; Zhang et al., 2019). Together, these findings suggest that simply reducing insulin production limits PanIN initiation in the context of obesity.

All cells in the body have insulin receptors and require insulin signaling for key functions, including nutrient uptake for storage and anabolism. While the roles of Insr in hepatocytes, myocytes, and adipocytes are well studied (Cen et al., 2022; Cherrington, 2005; Haeusler et al., 2018), the consequences of *Insr* loss in pancreatic acinar cells remain understudied. In this study, we specifically deleted the *Insr* gene from acinar cells using the *Ptf1a*^{CreER} allele and showed that insulin insensitivity in acinar cells had no obvious effects on systemic glucose homeostasis or serum insulin levels regardless of the *Kras* gene status. This suggests that the systemic regulation of glucose and insulin homeostasis are similarly perturbed in our mice fed HFD. Our data, combined with our previous studies (Zhang et al., 2022; Zhang et al., 2019), effectively rule out an essential role for hyperglycemia in PanIN and PDAC formation, but do not preclude potentially important roles for hyperglycemia in the later stages of disease (Sato et al., 2020; Vaziri-Gohar et al., 2022).

Insulin receptor signaling activates PI3K/AKT/mTOR and MAPK/ERK signaling cascades, both of which have mitogenic effects. Effector proteins in these two pathways are frequently mutated during tumorigenesis (Guo et al., 2020; Samuels et al., 2004; Yang et al., 2019), including in pancreatic cancer. Indeed, activating mutations in Kras, a key mediator of insulin and insulin-like growth factor signaling, drive the vast majority of pancreatic cancers (Waters and Der, 2018). Previous *in vitro* evidence supported the concept that hyperinsulinemia could promote cancer cell growth through over-activating the signaling cascades downstream of Insr protein (Chan et al., 2014b; Gallagher and LeRoith, 2020; Godsland, 2009; Zhang et al., 2021). Our findings are the first *in vivo* studies in any cancer type to demonstrate a direct causal role for hyperinsulinemia in the cancer cell of origin.

Mechanistically, our proteomic data demonstrated that *Insr* loss in acinar cells results in the coordinated reduction in digestive enzymes, with or without mutant Kras. This indicates that insulin signaling normally supports exocrine function. The reduced body weight in mice lacking acinar-cell Insr is also consistent with sub-clinical pancreatic insufficiency and a relative reduction in the ability to utilize ingested nutrients. Our observations are consistent with previous studies, including the observation that amylase production is diminished by β-cell ablation using streptozotocin and restored with insulin injection (Frier et al., 1976; Henderson et al., 1981; Soling and Unger, 1972). Mutations

that result in increased trypsin activity in the pancreas (Chang et al., 2017), as well as animal studies using the Cck analog, caerulein, to stimulate enzyme secretion at supraphysiological levels (Guerra et al., 2007), have demonstrated that tight control of digestive enzyme function reduces the risk of forming PDAC. Interestingly, our phospho-proteomic data identified hyper-phosphorylation of the Ccka receptor in Insr-knockout pancreas, linking local insulin signaling to Cck, a key endogenous regulator of acinar cell function and pancreatic weight. Cck secretion from I-cells is stimulated by the presence of amino acids and fat, which induces the highest I-cell secretion responses, in the small intestine (Otsuki, 2000). Cck affects pancreatic secretions predominately through local action on nerve fibres in the gut to induce a vago-vagal reflex circuit, resulting in acetylcholine secretion from nerves in the pancreas. Alternatively, it also can act directly on murine acinar cells through the Ccka receptor. In addition to mediating digestive enzyme release from acinar cells, previous studies have also shown that injecting low levels of Cck into mice results in increased pancreatic size over time (Dembinski and Johnson, 1980; Varga et al., 1988). This suggests that Cck helps regulate the enzyme production capacity of the pancreas. Finally, it has been reported that HFD-associated inflammation can also promote islet Cck expression, which was proposed to play a role in obesity-associated PanIN formation (Incio et al., 2016). However, our data indicate that hyperinsulinemia, acting through Insr, is the upstream driver of diet-induced inflammation via hyperactive digestive enzyme production. This supports a working model whereby hyperinsulinemia promotes PanIN initiation via increased local inflammation associated with elevated digestive enzyme production and/or release (Figure 8G). *Insr* loss in acinar cells counters the increased signal for acinar cell enzyme production or cell proliferation induced by HFD. Further studies are needed to fully understand the impact of dietary content on acinar cells and their susceptibility to $Kras^{G12D}$-mediated transformation.

Our proteomic analyses revealed other key mechanisms associated with suppressed pancreatic cancer initiation from acinar cells lacking *Insr*. For example, mRNA splicing and translation factors, known targets of insulin signaling (Haeusler et al., 2018), are differentially abundant in the pancreas after *Insr* loss in $Kras^{G12D}$-expressing acinar cells, suggesting possible mechanisms by which insulin might regulate the production of digestive enzymes. We also found evidence that reduced insulin

signaling affected cellular metabolism. Previous studies have suggested that insulin can promote glycolysis in wildtype acinar cells to protect them during pancreatitis (Bruce et al., 2021), however, detailed analyses of cell-type-specific mechanisms await single-cell cell proteomic and single-cell metabolomic characterization of this model.

We acknowledge the limitations of our study. One limitation of our study, and the field, is that existing antibody reagents are not specific enough to perform accurate anti-Insr staining that would allow us to determine whether acinar cells with normal morphology had escaped recombination at the *Insr* floxed allele. Another limitation is that, while our proteomic analysis provided quantification of 2889 protein abundances and 8787 phospho-sites, coverage of the proteome was not complete and biased against membrane proteins. For example, analysis of the abundance and phosphorylation of Igf1r, a protein that could compensate in *Insr* knockout cells, will require targeted assays and/or membrane fractionation. Insulin can bind to homodimeric Igf1 receptors and heterodimeric Insr/Igf1r hybrids, although at a lower affinity (Belfiore et al., 2009; Belfiore et al., 2017), to mediate its pro-tumourigenic effects. Nevertheless, it is clear that simply reducing *Insr* gene dosage was sufficient to reduce the effects of hyperinsulinemia on PanIN initiation. While we were unable to assess the role of Igf1r, future studies examining acinar cell-specific *Igf1r* loss in the presence or absence of concomitant *Insr* loss would be necessary to delineate any contribution to PanIN formation.

In summary, our data strongly suggest that insulin receptor signaling in acinar cells contributes to the PanIN and PDAC development. Our data illustrate the complex and interconnected molecular mechanisms by which hyperinsulinemia, acting directly through acinar cell Insr, promotes pancreatic tumourigenesis. We can infer that targeting insulin receptor signaling pathways, or hyperinsulinemia itself, may be beneficial in treating and preventing pancreatic cancer.

Methods

Mice

All animal experiments were conducted at the University of British Columbia with approval of the University of British Columbia Animal Care Committee in accordance with Canadian Council for Animal Care guidelines. All alleles have been described previously (Bruning et al., 1998; Kopp et al., 2012; Pan et al., 2013; Prigge et al., 2013; Søs Skovsø, 2021; Tuveson et al., 2004). *Kras*$^{LSL\text{-}G12D/w}$ (#008179), *Insr*$^{f/f}$ (#006955), and nuclear TdTomato-to-nuclear EGFP (nTnG) mice (#023035) were purchased from Jackson Labs (Bar Harbour, USA). *Ptf1a*$^{CreER/w}$ mice (C57BL/6) were a gift from Chris Wright (Vanderbilt, USA). Mice were maintained on C57BL/6 genetic background and housed at the University of British Columbia Modified Barrier Facility which was temperature-controlled and specific pathogen-free. They were kept on a 12:12 hr light: dark cycle with food and drinking water *ad libitum*. To generate genetic background-matched *Ptf1a*$^{CreER/w}$;*Kras*$^{LSL\text{-}G12D/w}$;*Insr*$^{w/w}$;nTnG, *Ptf1a*$^{CreER/w}$;*Kras*$^{LSL\text{-}G12D/w}$;*Insr*$^{w/f}$;nTnG, and *Ptf1a*$^{CreER/w}$;*Kras*$^{LSL\text{-}G12D/w}$;*Insr*$^{f/f}$;nTnG mice, *Ptf1a*$^{CreER/w}$;*Kras*$^{LSL\text{-}G12D/w}$;*Insr*$^{w/f}$;nTnG mice were bred with *Insr*$^{w/f}$ mice. After weaning (3 weeks), the resulting litters were fed with high fat diet (HFD), and at 4 weeks of age, recombination was induced over three consecutive days by subcutaneous injections of tamoxifen in corn oil (20 mg/mL) of 5 mg tamoxifen/40 g body mass. One cohort of mice was euthanized at 10 months of age for histopathology analyses and the whole pancreas was used for histopathology analyses. Another cohort of mice was euthanized at 12 weeks of age. For mice euthanized at 12 weeks, each pancreas was cut into three pieces roughly based on the pancreas anatomical structure: head, body, and tail. The body piece was used for histopathological analyses, while the other pieces were snap frozen in liquid nitrogen and kept at -80^{o}C. The head piece was processed for proteomics and phospho-proteomics analyses (see below).

Assessment of glucose homeostasis

Mouse body weight and fasting blood glucose levels were measured every 4 weeks and fasting insulin were measured every 3 months. Before the measurements, mice were fasted for 4 hours in clean and fresh cages during the light period. One drop of blood was collected from each mouse's

saphenous vein and a Lifescan OneTouch Ultra Mini glucometer was used to measure the fasting blood glucose levels. About 30 µl of blood was collected with a heparinized microhematocrit capillary tube (Fisher Scientific, 22-362566, Waltham, MA, USA) for measuring fasting insulin levels. The collected blood was centrifuged at 10,000 rpm for 10 minutes to collect the blood serum. Then the blood serum was kept at -20^{o}C until used to measure the fasting insulin levels with insulin ELISA (80-INSMSU-E10; ALPCO Diagnostics, Salem, NH).

Histopathological, morphological, and immunohistochemical analyses

Pancreata were fixed in 4% paraformaldehyde for 24 hours followed by paraffin embedding. Mouse pancreata were sectioned then stained with hematoxylin and eosin (H&E), and Alcian blue as previously described (Lee et al., 2018; Zhang et al., 2022; Zhang et al., 2019). The stained slides were scanned with a 20x objective using a 3DHISTECH Panoramic MIDI (Quorum Technologies Inc. Guelph, Canada) slide scanner. Histopathological analyses were conducted in a de-identified manner and verified separately by J.L.K and D.F.S. All histopathological analyses were performed on one of the stained sections that displayed the maximal pancreatic cross-sectional area unless otherwise stated. Every gland with a lumen was categorized as normal, ADM, PanIN, or neoplasia, and glands representing more than one of these categories were scored based on their highest-grade feature. The total pancreatic area, PanIN plus tumor area, PanIN area, and normal acinar cell area were measured as previously described (Zhang et al., 2022; Zhang et al., 2019). Briefly, the total pancreatic area, PanIN plus tumor area, PanIN area, normal acinar cell area was determined by masking all pancreatic tissue, selective masking of the PanIN plus tumor area, selective masking of the only PanIN area, and selective masking of the normal acinar cell area by Adobe Photoshop. Pixels for the total pancreatic area or each histological feature were measured by ImageJ and this was used to calculate the percentage area occupied by each histological feature. For Alcian blue positive area, Adobe Photoshop 2020 Black & White function was used to highlight the blue area (red filter). The total pixels for pancreas or Alcian blue positive area were counted using ImageJ.

Immunohistochemical (IHC) staining was performed according to published standard protocols (Lee et al., 2018; Zhang et al., 2022). Primary antibodies were rabbit anti-cytokeratin 19 (Ck19) (Abcam, ab133496, 1:1000) and goat anti-GFP (Abcam, ab6673, 1:200). Secondary antibodies were biotin-conjugated donkey anti-rabbit (Jackson ImmunoResearch Laboratories, Inc., 711-065-152, 1:500) and biotin-conjugated rat anti-goat (Vector Laboratories, MP-7404, 1:2). IHC slides were scanned with a 20x objective using a 3DHISTECH Panoramic MIDI slide scanner. Ck19 positive area was measured with Adobe Photoshop 2020 using the Black & White function to filter and highlight the brown area (blue filter), which was then taken as a percent of pixels in the pancreatic section.

Proteomics analyses

The whole head of pancreata collected from female mice at 12 weeks of age (*Ptf1a*^{CreER};*Kras*$^{LSL-G12D}$;*Insr*$^{w/w}$;nTnG (n=3), *Ptf1a*^{CreER};*Kras*$^{LSL-G12D}$;*Insr*$^{w/f}$;nTnG (n=6), *Ptf1a*^{CreER};*Kras*$^{LSL-G12D}$;*Insr*$^{f/f}$;nTnG (n=6), *Ptf1a*^{CreER};*Insr*$^{w/w}$;nTnG (n=3), and *Ptf1a*^{CreER};*Insr*$^{f/f}$;nTnG (n=2) mice) were frozen and used for (phospho)proteomic analyses. The frozen sample was ground into powder in a liquid nitrogen-cooled mortar and pestle and kept on dry ice until mass-spec analysis. Proteins were extracted from cryopulverized tumors in a buffer containing 5% sodium dodecyl sulfate (SDS) and 100 mM TRIS pH 7.8 supplemented with PhosStop phosphatase inhibitor cocktail (Roche). The protein concentration of the lysate was determined using bicinchoninic acid assay (BCA) (Thermo Fisher Scientific), and protein disulfide bonds were reduced and free Cysteines alkylated with 20 mM tris(2-carboxyethyl)phosphine (TCEP) and 30 mM iodoacetamide, respectively. 250 µg of total protein was used for proteolytic digestion using S-TRAP Mini columns (Protifi LLC, Huntington NY) (HaileMariam et al., 2018). Resultant tryptic peptides were then vacuum concentrated and desalted using Oasis HLB SPE cartridges (Waters). Peptides were vacuum concentrated and reconstituted in 0.1% trifluoro acetic acid (TFA), and 10% of the total sample was reserved for measurement of the total proteome. The remaining 90% of the sample was diluted in 80% acetonitrile with 0.1% TFA for automated phosphopeptide enrichment using AssayMap Fe-NTA (III) immobilized metal affinity chromatography

(IMAC) cartridges and a Bravo liquid handling system using the phosphopeptide enrichment v 2.1 application (Agilent).

LC-MS/MS acquisition and data analysis

Samples for both total proteomics and phosphoproteomics were analyzed by data dependent acquisition (DDA) using an Easy-nLC 1200 and Q Exactive Plus (both Thermo Fisher Scientific). Samples were first loaded onto a precolumn (Acclaim PepMap 100 C18, 3 µm particle size, 75 µm inner diameter x 2 cm) in 0.1% formic acid (buffer A), and gradient elution was performed using a 100-min method from 3 to 40% buffer B (84% acetonitrile, 0.1% formic acid) on the analytical column (Acclaim PepMap 100 C18, 2 µm particle size, 75 µm inner diameter x 25 cm) at a flow rate of 300 nL/min. MS scans were acquired between 350-1,500 m/z at a resolution of 70,000, with an automatic gain control (AGC) target of 1 x 10e610E6 ions and a maximum injection time of 50 ms. The top 15 precursor ions with charge states +2, +, +3, and +4 were isolated with a window of 1.2 m/z, an AGC target of 2 x 10e410E4 and a maximum injection time of 64 ms and fragmented using a normalized collision energy (NCE) of 28. MS/MS were acquired at a resolution of 17,500 and the dynamic exclusion was set to 30 s. DDA MS raw data was processed with Proteome Discoverer 2.5 (Thermo Scientific) and searched using Sequest HT against the mouse reference proteome FASTA database from Uniprot (downloaded October 1st 2021; 17,054 forward sequences). The enzyme specificity was set to trypsin with a maximum of 2 missed cleavages. Carbamidomethylation of cysteine was set as a fixed modification and oxidation of methionine, as well as phosphorylation of serine, threonine, and tyrosine as variable modifications. The precursor ion mass tolerance was set to 10 parts per million, and the product ion mass tolerance was set to 0.02 Da. Percolator was used to assess posterior error probabilities and the data was filtered using a false discovery rate (FDR) of <1% on peptide and protein level. The Minora node of Proteome Discoverer was used for label free quantitation. For the new human comparison, Pathway enrichment was performed our mouse data and PDAC human data (Cao et al., 2021) using Reactome (v80) (Gillespie et al., 2022). We performed differential abundance analysis on the human data using the R package limma (Ritchie et al., 2015). For our data, we used a

565 cutoff of Adj. p<0.05. For the human data, we used Adj. p<1e-19 and 1e-12 for the total proteins and
566 phospho-proteins respectively to ensure a comparable proportion of the total number detected.
567
568 **Primary mouse acinar cell isolation and three-dimensional culture**
569 Primary pancreatic acinar cells were isolated from pancreata of wild-type female mice at the age of
570 6-8 weeks. The acinar cell isolation procedure was adapted from the protocol described by Martinez
571 and Storz (Fleming Martinez and Storz, 2019). Briefly, the mouse pancreas was harvested and
572 washed three times in 1x HBSS, which were then minced into 1-5mm pieces. The fragmented tissue
573 was then digested with 5mL (0.4mg/mL) collagenase P in 37 °C with gentle shaking for 18 minutes.
574 HBSS (10mL) with 5% FBS was added to terminate the digestion reaction, followed by 3 washes with
575 10mL HBSS (5% FBS) to remove the residual collagenase P. After each wash, the tissue was pelleted
576 (450g RCF, 2 min at room temperature) and the supernatant was removed. The digested tissue was
577 resuspended in 10mL HBSS (5% FBS) and filtered through a 100 μM cell strainer, followed by a wash
578 with 10mL HBSS (5% FBS). The filtrate was gently added to 20mL HBSS 30% FBS cushion to form
579 layers of cells. The cell mixture was centrifuged at 180g RCF at room temperature for 2 minutes to
580 pellet acinar cells. Appropriate number of acinar cells were then resuspended in premade collagen
581 solution (1mg/ml rat tail type1 collagen, 10x Waymouth's media, RPMI1640 complete media (1% FBS,
582 1x penicillin/streptomycin, 1μg/mL dexamethasone), adjusted to pH = ~7.8 with 1M NaOH) and plated
583 (50μL per well) in collagen pre-coated 96-well plates. After solidification, 100 μL of the RPMI1640
584 complete media with insulin (0.1nM-100nM), TGF-α (50ng/mL) or combined treatments, with or
585 without 0.1mg/mL soybean trypsin inhibitor was added. Media was replaced on day 1 and 3, and the
586 numbers of ADM events in each well were quantified on day 5. Isolated cells were maintained at 37 ^{o}C
587 in a humidified incubator with 5% CO_2.
588
589 **Statistical analyses and data visualization**
590 Animals were excluded from the histopathological analyses if they were found dead or if nTnG
591 recombination efficiency (% acinar cells or PanIN cells labeled with GFP) was lower than 20%.

Statistical analyses were conducted with GraphPad Prism 9.3.0. The Shapiro-Wilk test was used to assess data normality. One-way ANOVA was performed unless otherwise stated. Mixed-effect analyses were run for glucose homeostasis data (mouse body weight, fasting glucose level, and fasting insulin level). When comparing the histopathological measurements between male and female mice from the same genotype, a two-tailed student's t-test was run for normally distributed data and a Mann-Whitney test was performed for non-normally distributed data. Statistical parameters, including the exact value of sample size n (animal number), precision measures and dispersion (mean ± SEM), and statistical significance levels, are reported in the Figures and Figure legends. A p-value <0.05 was considered significant. In Figures, asterisks denote statistical significance (*p<0.05, **p<0.01, ***p<0.001, and ****p<0.0001).

For total proteomics data, normalization, imputation, and differential expression analyses were performed on the protein abundances using Proteome Discoverer. Differential expression analysis used background-based t-tests with p-values adjusted using Benjamini-Hochberg correction. The proteins were filtered for significant comparisons (Adj. p<0.05), and heatmaps were created with resultant protein lists. We also applied k-means clustering and extracted clusters with patterns of interest (Gu et al., 2016). From this heatmap, a class of specific secreted proteins were identified and values for all samples were plotted in a heatmap and sorted with hierarchical clustering. We used STRING (v11) to generate an edge table with differentially expressed total proteins (Adj. p<0.05) with an absolute $\log_2$(Fold Change) cut-off of 2.5 in *Ptf1a*^{CreER};*Kras*$^{LSL\text{-}G12D}$;*Insr*$^{w/w}$;nTnG compared to *Ptf1a*^{CreER};*Kras*$^{LSL\text{-}G12D}$;*Insr*$^{f/f}$;nTnG. Protein-protein relationships were only included if they involved experimental evidence or interactions annotated in other databases (Szklarczyk et al., 2021). Cytoscape (v3.9.1) was used to visualize the network (Shannon et al., 2003), with background images created with BioRender.com.

Phospho-proteomics data were analyzed two ways. In the first approach, we only used phospho-peptides with measurements made in a minimum of 2/3 of all the samples and at least one sample per group. We imputed missing phospho-protein values in samples before normalization and statistical analysis using the same process as the total proteomics, allowing a broader assessment of the

phospho-protein landscape. These were plotted using volcano plots and against the corresponding proteins in the total protein data set with calculated $\log_2$(Fold Change) of the median. In the second approach, we aggregated the abundances of each sample for each phospho-site detected, and normalized each of the detected phospho-sites to the total abundance of the corresponding protein. We only included phospho-sites where every sample had an experimentally measured total protein value. The second method used differential expression analysis performed using the R package limma on the *Ptf1a*^{CreER};*Kras*$^{LSL\text{-}G12D}$;*Insr*$^{w/w}$;nTnG vs *Ptf1a*^{CreER};*Kras*$^{LSL\text{-}G12D}$;*Insr*$^{f/f}$;nTnG comparison (Ritchie et al., 2015). The top differentially abundant phospho-sites (sorted by Adj. p-value) were plotted as a heatmap and sorted with hierarchical clustering (Gu et al., 2016). Phosphosite (www.phosphosite.org) was used to determine upstream activators, cellular location, and function of each protein, as well as the specific kinases of the detected phospho-sites (if known). STRING was used to identify proteins that physically interact with each other (Szklarczyk et al., 2021).

References

Aljada, A., Saleh, A. M., Al-Aqeel, S. M., Shamsa, H. B., Al-Bawab, A., Al Dubayee, M., and Ahmed, A. A. (2015). Quantification of insulin receptor mRNA splice variants as a diagnostic tumor marker in breast cancer. Cancer Biomark *15*, 653-661.

Belfiore, A., Frasca, F., Pandini, G., Sciacca, L., and Vigneri, R. (2009). Insulin receptor isoforms and insulin receptor/insulin-like growth factor receptor hybrids in physiology and disease. Endocr Rev *30*, 586-623.

Belfiore, A., Malaguarnera, R., Vella, V., Lawrence, M. C., Sciacca, L., Frasca, F., Morrione, A., and Vigneri, R. (2017). Insulin Receptor Isoforms in Physiology and Disease: An Updated View. Endocr Rev *38*, 379-431.

Berglund, E. D., Li, C. Y., Poffenberger, G., Ayala, J. E., Fueger, P. T., Willis, S. E., Jewell, M. M., Powers, A. C., and Wasserman, D. H. (2008). Glucose metabolism in vivo in four commonly used inbred mouse strains. Diabetes *57*, 1790-1799.

Binder, J. X., Pletscher-Frankild, S., Tsafou, K., Stolte, C., O'Donoghue, S. I., Schneider, R., and Jensen, L. J. (2014). COMPARTMENTS: unification and visualization of protein subcellular localization evidence. Database (Oxford) *2014*, bau012.

Bruce, J. I. E., Sanchez-Alvarez, R., Sans, M. D., Sugden, S. A., Qi, N., James, A. D., and Williams, J. A. (2021). Insulin protects acinar cells during pancreatitis by preserving glycolytic ATP supply to calcium pumps. Nat Commun *12*, 4386.

Bruning, J. C., Michael, M. D., Winnay, J. N., Hayashi, T., Horsch, D., Accili, D., Goodyear, L. J., and Kahn, C. R. (1998). A muscle-specific insulin receptor knockout exhibits features of the metabolic syndrome of NIDDM without altering glucose tolerance. Mol Cell *2*, 559-569.

Cao, L., Huang, C., Cui Zhou, D., Hu, Y., Lih, T. M., Savage, S. R., Krug, K., Clark, D. J., Schnaubelt, M., Chen, L.*, et al.* (2021). Proteogenomic characterization of pancreatic ductal adenocarcinoma. Cell *184*, 5031-5052 e5026.

Cen, H. H., Hussein, B., Botezelli, J. D., Wang, S., Zhang, J. A., Noursadeghi, N., Jessen, N., Rodrigues, B., Timmons, J. A., and Johnson, J. D. (2022). Human and mouse muscle transcriptomic analyses identify insulin receptor mRNA downregulation in hyperinsulinemia-associated insulin resistance. FASEB J *36*, e22088.

Chan, D. S., Vieira, A. R., Aune, D., Bandera, E. V., Greenwood, D. C., McTiernan, A., Navarro Rosenblatt, D., Thune, I., Vieira, R., and Norat, T. (2014a). Body mass index and survival in women with breast cancer-systematic literature review and meta-analysis of 82 follow-up studies. Ann Oncol *25*, 1901-1914.

Chan, M. T., Lim, G. E., Skovso, S., Yang, Y. H., Albrecht, T., Alejandro, E. U., Hoesli, C. A., Piret, J. M., Warnock, G. L., and Johnson, J. D. (2014b). Effects of insulin on human pancreatic cancer progression modeled in vitro. BMC Cancer *14*, 814.

Chang, H. H., Moro, A., Takakura, K., Su, H. Y., Mo, A., Nakanishi, M., Waldron, R. T., French, S. W., Dawson, D. W., Hines, O. J.*, et al.* (2017). Incidence of pancreatic cancer is dramatically increased by a high fat, high calorie diet in KrasG12D mice. PLoS One *12*, e0184455.

671 Chen, Z., Downing, S., and Tzanakakis, E. S. (2019). Four Decades After the Discovery of
672 Regenerating Islet-Derived (Reg) Proteins: Current Understanding and Challenges. Front Cell Dev
673 Biol *7*, 235.

674 Cherrington, A. D. (2005). The role of hepatic insulin receptors in the regulation of glucose production.
675 J Clin Invest *115*, 1136-1139.

676 Dawson, D. W., Hertzer, K., Moro, A., Donald, G., Chang, H. H., Go, V. L., Pandol, S. J., Lugea, A.,
677 Gukovskaya, A. S., Li, G.*, et al.* (2013). High-fat, high-calorie diet promotes early pancreatic neoplasia
678 in the conditional KrasG12D mouse model. Cancer Prev Res (Phila) *6*, 1064-1073.

679 Dembinski, A. B., and Johnson, L. R. (1980). Stimulation of Pancreatic Growth by Secretin, Caerulein,
680 and Pentagastrin. Endocrinology *106*, 323-328.

681 Fleming Martinez, A. K., and Storz, P. (2019). Mimicking and Manipulating Pancreatic Acinar-to-Ductal
682 Metaplasia in 3-dimensional Cell Culture. J Vis Exp.

683 Frier, B. M., Saunders, J. H., Wormsley, K. G., and Bouchier, I. A. (1976). Exocrine pancreatic function
684 in juvenile-onset diabetes mellitus. Gut *17*, 685-691.

685 Gallagher, E. J., and LeRoith, D. (2020). Hyperinsulinaemia in cancer. Nat Rev Cancer *20*, 629-644.

686 Gillespie, M., Jassal, B., Stephan, R., Milacic, M., Rothfels, K., Senff-Ribeiro, A., Griss, J., Sevilla, C.,
687 Matthews, L., Gong, C.*, et al.* (2022). The reactome pathway knowledgebase 2022. Nucleic Acids Res
688 *50*, D687-D692.

689 Godsland, I. F. (2009). Insulin resistance and hyperinsulinaemia in the development and progression
690 of cancer. Clin Sci (Lond) *118*, 315-332.

691 Gu, Z., Eils, R., and Schlesner, M. (2016). Complex heatmaps reveal patterns and correlations in
692 multidimensional genomic data. Bioinformatics *32*, 2847-2849.

693 Guerra, C., Schuhmacher, A. J., Cañamero, M., Grippo, P. J., Verdaguer, L., Pérez-Gallego, L.,
694 Dubus, P., Sandgren, E. P., and Barbacid, M. (2007). Chronic pancreatitis is essential for induction of
695 pancreatic ductal adenocarcinoma by K-Ras oncogenes in adult mice. Cancer Cell *11*, 291-302.

696 Guo, Y. J., Pan, W. W., Liu, S. B., Shen, Z. F., Xu, Y., and Hu, L. L. (2020). ERK/MAPK signalling
697 pathway and tumorigenesis. Exp Ther Med *19*, 1997-2007.

698 Haeusler, R. A., McGraw, T. E., and Accili, D. (2018). Biochemical and cellular properties of insulin
699 receptor signalling. Nat Rev Mol Cell Biol *19*, 31-44.

700 HaileMariam, M., Eguez, R. V., Singh, H., Bekele, S., Ameni, G., Pieper, R., and Yu, Y. (2018). S-Trap,
701 an Ultrafast Sample-Preparation Approach for Shotgun Proteomics. J Proteome Res *17*, 2917-2924.

702 Haoning Howard Cen, J. R., Libin Abraham, Michael R. Gold, Leonard J. Foster, James D. Johnson
703 (2022). Insulin-dependent and -independent dynamics of insulin receptor trafficking in muscle cells.
704 bioRxiv.

705 Heestand, G. M., and Kurzrock, R. (2015). Molecular landscape of pancreatic cancer: implications for
706 current clinical trials. Oncotarget *6*, 4553-4561.

707 Henderson, J. R., Daniel, P. M., and Fraser, P. A. (1981). The pancreas as a single organ: the
708 influence of the endocrine upon the exocrine part of the gland. Gut *22*, 158-167.

Hernandez, V. J., Weng, J., Ly, P., Pompey, S., Dong, H., Mishra, L., Schwarz, M., Anderson, R. G., and Michaely, P. (2013). Cavin-3 dictates the balance between ERK and Akt signaling. Elife *2*, e00905.

Hong, S., Freeberg, M. A., Han, T., Kamath, A., Yao, Y., Fukuda, T., Suzuki, T., Kim, J. K., and Inoki, K. (2017). LARP1 functions as a molecular switch for mTORC1-mediated translation of an essential class of mRNAs. Elife *6*.

Hopkins, B. D., Pauli, C., Du, X., Wang, D. G., Li, X., Wu, D., Amadiume, S. C., Goncalves, M. D., Hodakoski, C., Lundquist, M. R.*, et al.* (2018). Suppression of insulin feedback enhances the efficacy of PI3K inhibitors. Nature *560*, 499-503.

Ilic, M., and Ilic, I. (2016). Epidemiology of pancreatic cancer. World J Gastroenterol *22*, 9694-9705.

Incio, J., Liu, H., Suboj, P., Chin, S. M., Chen, I. X., Pinter, M., Ng, M. R., Nia, H. T., Grahovac, J., Kao, S.*, et al.* (2016). Obesity-Induced Inflammation and Desmoplasia Promote Pancreatic Cancer Progression and Resistance to Chemotherapy. Cancer Discov *6*, 852-869.

Janku, F., Wheler, J. J., Naing, A., Falchook, G. S., Hong, D. S., Stepanek, V. M., Fu, S., Piha-Paul, S. A., Lee, J. J., Luthra, R.*, et al.* (2013). PIK3CA mutation H1047R is associated with response to PI3K/AKT/mTOR signaling pathway inhibitors in early-phase clinical trials. Cancer Res *73*, 276-284.

Kopp, J. L., von Figura, G., Mayes, E., Liu, F. F., Dubois, C. L., Morris, J. P. t., Pan, F. C., Akiyama, H., Wright, C. V., Jensen, K.*, et al.* (2012). Identification of Sox9-dependent acinar-to-ductal reprogramming as the principal mechanism for initiation of pancreatic ductal adenocarcinoma. Cancer Cell *22*, 737-750.

Law, J. H., Habibi, G., Hu, K., Masoudi, H., Wang, M. Y., Stratford, A. L., Park, E., Gee, J. M., Finlay, P., Jones, H. E.*, et al.* (2008). Phosphorylated insulin-like growth factor-i/insulin receptor is present in all breast cancer subtypes and is related to poor survival. Cancer Res *68*, 10238-10246.

Lee, A. Y. L., Dubois, C. L., Sarai, K., Zarei, S., Schaeffer, D. F., Sander, M., and Kopp, J. L. (2018). Cell of origin affects tumour development and phenotype in pancreatic ductal adenocarcinoma. Gut.

Li, Q., Wang, H., Zogopoulos, G., Shao, Q., Dong, K., Lv, F., Nwilati, K., Gui, X. Y., Cuggia, A., Liu, J. L., and Gao, Z. H. (2016). Reg proteins promote acinar-to-ductal metaplasia and act as novel diagnostic and prognostic markers in pancreatic ductal adenocarcinoma. Oncotarget *7*, 77838-77853.

Means, A. L., Meszoely, I. M., Suzuki, K., Miyamoto, Y., Rustgi, A. K., Coffey, R. J., Jr., Wright, C. V., Stoffers, D. A., and Leach, S. D. (2005a). Pancreatic epithelial plasticity mediated by acinar cell transdifferentiation and generation of nestin-positive intermediates. Development *132*, 3767-3776.

Means, A. L., Meszoely, I. M., Suzuki, K., Miyamoto, Y., Rustgi, A. K., Coffey, R. J., Wright, C. V. E., Stoffers, D. A., and Leach, S. D. (2005b). Pancreatic epithelial plasticity mediated by acinar cell transdifferentiation and generation of nestin-positive intermediates. Development (Cambridge, England) *132*, 3767-3776.

Mehran, A. E., Templeman, N. M., Brigidi, G. S., Lim, G. E., Chu, K. Y., Hu, X., Botezelli, J. D., Asadi, A., Hoffman, B. G., Kieffer, T. J.*, et al.* (2012). Hyperinsulinemia drives diet-induced obesity independently of brain insulin production. Cell Metab *16*, 723-737.

Muzumdar, M. D., Tasic, B., Miyamichi, K., Li, L., and Luo, L. (2007). A global double-fluorescent Cre reporter mouse. Genesis *45*, 593-605.

Otsuki, M. (2000). Pathophysiological role of cholecystokinin in humans. J Gastroenterol Hepatol *15 Suppl*, D71-83.

Pan, F. C., Bankaitis, E. D., Boyer, D., Xu, X., Van de Casteele, M., Magnuson, M. A., Heimberg, H., and Wright, C. V. (2013). Spatiotemporal patterns of multipotentiality in Ptf1a-expressing cells during pancreas organogenesis and injury-induced facultative restoration. Development *140*, 751-764.

Payne, S. N., Maher, M. E., Tran, N. H., Van De Hey, D. R., Foley, T. M., Yueh, A. E., Leystra, A. A., Pasch, C. A., Jeffrey, J. J., Clipson, L.*, et al.* (2015). PIK3CA mutations can initiate pancreatic tumorigenesis and are targetable with PI3K inhibitors. Oncogenesis *4*, e169.

Pisani, P. (2008). Hyper-insulinaemia and cancer, meta-analyses of epidemiological studies. Arch Physiol Biochem *114*, 63-70.

Prigge, J. R., Wiley, J. A., Talago, E. A., Young, E. M., Johns, L. L., Kundert, J. A., Sonsteng, K. M., Halford, W. P., Capecchi, M. R., and Schmidt, E. E. (2013). Nuclear double-fluorescent reporter for in vivo and ex vivo analyses of biological transitions in mouse nuclei. Mamm Genome.

Rahib, L., Smith, B. D., Aizenberg, R., Rosenzweig, A. B., Fleshman, J. M., and Matrisian, L. M. (2014). Projecting cancer incidence and deaths to 2030: the unexpected burden of thyroid, liver, and pancreas cancers in the United States. Cancer Res *74*, 2913-2921.

Rao, R. V., Holicky, E. L., Kuntz, S. M., and Miller, L. J. (2000). CCK receptor phosphorylation exposes regulatory domains affecting phosphorylation and receptor trafficking. Am J Physiol Cell Physiol *279*, C1986-1992.

Ritchie, M. E., Phipson, B., Wu, D., Hu, Y., Law, C. W., Shi, W., and Smyth, G. K. (2015). limma powers differential expression analyses for RNA-sequencing and microarray studies. Nucleic Acids Res *43*, e47.

Samuels, Y., Wang, Z., Bardelli, A., Silliman, N., Ptak, J., Szabo, S., Yan, H., Gazdar, A., Powell, S. M., Riggins, G. J.*, et al.* (2004). High frequency of mutations of the PIK3CA gene in human cancers. Science *304*, 554.

Sato, K., Hikita, H., Myojin, Y., Fukumoto, K., Murai, K., Sakane, S., Tamura, T., Yamai, T., Nozaki, Y., Yoshioka, T.*, et al.* (2020). Hyperglycemia enhances pancreatic cancer progression accompanied by elevations in phosphorylated STAT3 and MYC levels. PloS one *15*, e0235573-e0235573.

Shannon, P., Markiel, A., Ozier, O., Baliga, N. S., Wang, J. T., Ramage, D., Amin, N., Schwikowski, B., and Ideker, T. (2003). Cytoscape: a software environment for integrated models of biomolecular interaction networks. Genome Res *13*, 2498-2504.

Sivaram, N., McLaughlin, P. A., Han, H. V., Petrenko, O., Jiang, Y. P., Ballou, L. M., Pham, K., Liu, C., van der Velden, A. W., and Lin, R. Z. (2019). Tumor-intrinsic PIK3CA represses tumor immunogenecity in a model of pancreatic cancer. J Clin Invest *129*, 3264-3276.

Smith, J. P., and Solomon, T. E. (2014). Cholecystokinin and pancreatic cancer: the chicken or the egg? Am J Physiol Gastrointest Liver Physiol *306*, G91-G101.

Soling, H. D., and Unger, K. O. (1972). The role of insulin in the regulation of -amylase synthesis in the rat pancreas. Eur J Clin Invest *2*, 199-212.

Søs Skovsø, E. P., Jelena Kolic, Haoning Howard Cen, Derek A. Dionne, Xiao-Qing Dai, Rohit B. Sharma, Lynda Elghazi, Cara E. Ellis, Katharine Faulkner, Stephanie A.M. Marcil, Peter Overby, Nilou

Noursadeghi, Daria Hutchinson, Xiaoke Hu, Hong Li, Honey Modi, Jennifer S. Wildi, J. Diego Botezelli, Hye Lim Noh, Sujin Suk, Brian Gablaski, Austin Bautista, Ryekjang Kim, Cras-Méneur, Stephane Flibotte, Sunita Sinha, Dan S. Luciani, Corey Nislow, Elizabeth J. Rideout, Eric N. Cytrynbaum, Jason K. Kim, Ernesto Bernal-Mizrachi, Laura C. Alonso, Patrick E. MacDonald, James D. Johnson (2021). Beta-cell specific Insr deletion promotes insulin hypersecretion and improves glucose tolerance prior to global insulin resistance. biRxiv.

Steiner, S., Seleznik, G. M., Reding, T., Stopic, M., Lenggenhager, D., Ten Buren, E., Eshmuminov, D., Endhardt, K., Hagedorn, C., Heidenblut, A. M*., et al.* (2022). De novo expression of gastrokines in pancreatic precursor lesions impede the development of pancreatic cancer. Oncogene *41*, 1507-1517.

Stolzenberg-Solomon, R. Z., Graubard, B. I., Chari, S., Limburg, P., Taylor, P. R., Virtamo, J., and Albanes, D. (2005). Insulin, glucose, insulin resistance, and pancreatic cancer in male smokers. JAMA *294*, 2872-2878.

Szklarczyk, D., Gable, A. L., Nastou, K. C., Lyon, D., Kirsch, R., Pyysalo, S., Doncheva, N. T., Legeay, M., Fang, T., Bork, P*., et al.* (2021). The STRING database in 2021: customizable protein-protein networks, and functional characterization of user-uploaded gene/measurement sets. Nucleic Acids Res *49*, D605-D612.

Templeman, N. M., Clee, S. M., and Johnson, J. D. (2015). Suppression of hyperinsulinaemia in growing female mice provides long-term protection against obesity. Diabetologia *58*, 2392-2402.

Templeman, N. M., Flibotte, S., Chik, J. H. L., Sinha, S., Lim, G. E., Foster, L. J., Nislow, C., and Johnson, J. D. (2017). Reduced Circulating Insulin Enhances Insulin Sensitivity in Old Mice and Extends Lifespan. Cell Rep *20*, 451-463.

Tuveson, D. A., Shaw, A. T., Willis, N. A., Silver, D. P., Jackson, E. L., Chang, S., Mercer, K. L., Grochow, R., Hock, H., Crowley, D*., et al.* (2004). Endogenous oncogenic K-ras(G12D) stimulates proliferation and widespread neoplastic and developmental defects. Cancer Cell *5*, 375-387.

Varga, G., Papp, M., Solomon, T. E., Scarpignato, C., Toth, I. E., and Szabo, D. (1988). Caerulein in supramaximal doses fails to stimulate pancreatic growth, but it forces secretory granulopoiesis. Acta Physiol Hung *71*, 99-106.

Vaziri-Gohar, A., Hue, J. J., Graor, H. G., Abbas, A., Zarei, M., Hajihassani, O., Titomihelakis, G., Feczko, J., Rathore, M., Wang, R*., et al.* (2022). Increased glucose availability sensitizes pancreatic cancer to chemotherapy. bioRxiv, 2022.2004.2029.490090.

Waters, A. M., and Der, C. J. (2018). KRAS: The Critical Driver and Therapeutic Target for Pancreatic Cancer. Cold Spring Harb Perspect Med *8*.

Yang, J., Nie, J., Ma, X., Wei, Y., Peng, Y., and Wei, X. (2019). Targeting PI3K in cancer: mechanisms and advances in clinical trials. Mol Cancer *18*, 26.

Zhang, A. M. Y., Chu, K. H., Daly, B. F., Ruiter, T., Dou, Y., Yang, J. C. C., de Winter, T. J. J., Chhuor, J., Wang, S., Flibotte, S*., et al.* (2022). Effects of hyperinsulinemia on pancreatic cancer development and the immune microenvironment revealed through single-cell transcriptomics. Cancer Metab *10*, 5.

Zhang, A. M. Y., Magrill, J., de Winter, T. J. J., Hu, X., Skovsø, S., Schaeffer, D. F., Kopp, J. L., and Johnson, J. D. (2019). Endogenous Hyperinsulinemia Contributes to Pancreatic Cancer Development. Cell Metab *30*, 403-404.

828 Zhang, A. M. Y., Wellberg, E. A., Kopp, J. L., and Johnson, J. D. (2021). Hyperinsulinemia in Obesity,
829 Inflammation, and Cancer. Diabetes Metab J *45*, 285-311.

830

Figure Legends

Fig. 1. Loss of *Insr* in pancreatic acinar cells had no effect on glucose homeostasis and pancreas size.

A, Schematic describing mouse models designed to test the role of insulin receptor signaling in pancreatic acinar cells. On the background of the *Ptf1a*^{CreER} mice, we generated mice having two wild-type *Insr* alleles (*Insr*$^{w/w}$) or two *Insr* floxed alleles (*Insr*$^{f/f}$). **B**, Three-week-old mice were weaned and provided high fat diet (HFD) for the duration of the study. At 4-weeks-old, they were injected with tamoxifen (TM) on 3 consecutive days. Physiological measures were taken every 3 months for 10 months, mice were euthanized at 12 or 43.5 weeks of age for histopathological, proteomics, and phospho-proteomics analyses. **C-H,** Body weight (**C-D**), fasting blood glucose (**E-F**), and fasting insulin (**G-H**) measurements in male (**C, E, G**) and female (**D, F, H**) *Ptf1a*^{CreER}-*Insr*$^{w/w}$ and *Ptf1a*^{CreER}-*Insr*$^{f/f}$ mice measured over >1 year (n= 10-17). **I,** The ratio of pancreatic weight to mouse body weight for male (M) and female (F) *Ptf1a*^{CreER}-*Insr*$^{w/w}$ and *Ptf1a*^{CreER}-*Insr*$^{f/f}$ mice (n= 3-6). Values shown as mean ± SEM.

Fig. 2. Loss of *Insr* in pancreatic acinar cells had no effect on glucose homeostasis in *Ptf1a*^{CreER}-induced *Kras*^{G12D} pancreatic cancer model.

A, Schematic describing a mouse model designed to test the role of insulin receptor signaling on HFD-accelerated PDAC initiation. On the background of the *Ptf1a*^{CreER}-induced *Kras*^{G12D} pancreatic cancer model (PK), we generated mice having two wild-type *Insr* alleles (*Insr*$^{w/w}$), one *Insr* floxed allele (*Insr*$^{w/f}$), or two *Insr* floxed alleles (*Insr*$^{f/f}$). **B-G,** Body weight (**B-C),** fasting blood glucose (**D-F)**, or fasting insulin (**F-G)** measurements for PK-*Insr*$^{w/w}$, PK-*Insr*$^{w/f}$, and PK-*Insr*$^{f/f}$ male (**B, D, F**) and female (**C, E, G**) mice (n= 13-33). Values shown as mean ± SEM. *p<0.05.

Fig. 3. Loss of *Insr* in acinar cells reduced PanIN and PDAC formation.

A, Percentage of mice of the indicated genotype that were found dead or reached humane endpoint throughout the study. The star symbol indicates whether a macroscopic mass was observed in the

858 pancreas at necropsy, when possible. There were 8 PK-*Insr*$^{w/w}$, 20 PK-*Insr*$^{w/f}$, and 7 PK-*Insr*$^{f/f}$ male
859 mice and 9 PK-*Insr*$^{w/w}$ 17 PK-*Insr*$^{w/f}$, and 12 PK-*Insr*$^{f/f}$ female mice in the cohort. At 43.5 weeks, the
860 remaining mice were euthanized and assessed for presence of tumors. **B-C,** Representative whole
861 section (top) and high-magnification (bottom) H&E images of pancreatic slides from 43.5-week-old
862 male (**B**) and female (**C**) PK-*Insr*$^{w/w}$, PK-*Insr*$^{w/f}$, and PK-*Insr*$^{f/f}$ mice. **D-G,** Quantification of PanIN plus
863 tumor area (**D**)**,** PanIN only area (**E**), tumor area (**F**), or acinar cell area (**G**) in pancreata from each
864 genotype and sex (male or female) (n= 5-16). Filled dots and triangles denoted mice that developed
865 tumors in **D**. Scale bars: 2 mm (top) and 0.1mm (bottom). Values are shown as mean ± SEM. *p<0.05,
866 **p<0.01, ***p<0.001, ****p<0.0001.
867
868 **Fig. 4. Loss of *Insr* in acinar cells reduced PanIN lesions initiation.**
869 **A,** The ratio of pancreatic weight to mouse body weight for male (M) and female (F) PK-*Insr*$^{w/w}$, PK-
870 *Insr*$^{w/f}$, and PK-*Insr*$^{f/f}$ mice (n= 3-15). **B,** Quantification of PanIN area in pancreata from each genotype
871 and sex (male or female) (n= 3-14). **C-D,** Representative whole section (top) and high-magnification
872 (bottom) H&E images of pancreatic slides from 12-week-old male (**C**) and female (**D**) PK-*Insr*$^{w/w}$, PK-
873 *Insr*$^{w/f}$, and PK-*Insr*$^{f/f}$ mice. Scale bars: 2 mm (top) and 0.1mm (bottom). Values are shown as mean ±
874 SEM. *p<0.05, **p<0.01.
875
876 **Fig. 5. The proteomic analysis of insulin receptors' effects on PanIN initiation**
877 **A**, Volcano plot for proteins that were significantly up- or down-regulated in PK-*Insr*$^{w/w}$ mice (n=3)
878 compared to *Ptf1a*^{CreER}-*Insr*$^{w/w}$ mice (n=3). **B**, Volcano plot for proteins that were significantly up- or
879 down-regulated in *Ptf1a*^{CreER}-*Insr*$^{f/f}$ mice (n=2) compared to *Ptf1a*^{CreER}-*Insr*$^{w/w}$ mice (n=3). **C**, Volcano
880 plot showing proteins that were significantly up- or down-regulated in PK-*Insr*$^{f/f}$ mice compared to PK-
881 *Insr*$^{w/w}$ mice. **D,** Proteins that were differentially abundant between PK-*Insr*$^{w/w}$ and PK-*Insr*$^{f/f}$ mice were
882 selected and their abundance across all genotypes was used for k-means clustering. The clusters
883 were visualized by heatmap to show their variance across all genotypes. The proteins in clusters 1, 2,
884 3, and 7 are listed in the order shown in the heatmap from top to bottom.

Fig. 6. Loss of *Insr* in acinar cells reduced digestive enzymes production in pancreas.

A, Differentially abundant proteins between PK-*Insr*$^{w/w}$ and PK-*Insr*$^{f/f}$ pancreata were connected using STRING and diagrammatically presented here in the context of Insr signaling and cellular organelles and functions. The color in each oval reflects the fold change, while the thickness of the line around the oval represents the Adj. p-value. Proteins depicted in white ovals were added to show the potential relationship of the differentially abundant proteins to insulin signaling. **B**, Heatmap showing the change of protein abundance between genotypes for proteins involved in pancreatic digestive enzymes secretion. **C**, The percentage of summed digestive enzyme abundances in total measured proteins for each genotype. Values are shown as mean ± SEM. *p<0.05, **p<0.01.

Fig. 7. The phospho-proteomic analysis of insulin receptors' effects on PanIN initiation

A, Volcano plots for phospho-peptides that were significantly up or down regulated in PK-*Insr*$^{f/f}$ mice compared to PK-*Insr*$^{w/w}$ mice. **B**, Change in phospho-peptide abundance (Adj. p-values indicated in red) compared to the change in corresponding protein's abundance between PK-*Insr*$^{f/f}$ mice and PK-*Insr*$^{w/w}$ mice. **C**, TOP: Schematic of phosphorylation sites on Cckar that were differentially abundant in any comparison. BOTTOM: The relative phospho-peptide abundance (arbitrary units) for each detected phospho-peptide for all samples (white dots) and genotypes. **D,** Intracellular locations and functions of differentially abundant phospho-sites and their corresponding protein. The color in each attached phospho-site reflects the fold change, while the thickness of the border represents the Adj. p-value. Values are shown as mean ± SEM. *p<0.05, **p<0.01, ***p<0.001, ****p<0.0001.

Fig. 8. Insulin receptor signaling promotes PanIN initiation via increased inflammation associated with hyperactive digestive enzyme production.

A-B, Representative whole section (top) and high-magnification (bottom) images of pancreatic slides from 12-week-old male (**A**) and female (**B**) mice PK-*Insr*$^{w/w}$, PK-*Insr*$^{w/f}$, and PK-*Insr*$^{f/f}$ stained with Sirius red. **C,** Quantification of Sirius red positive area for mice from each genotype and sex (male (M) or female (F)) (n= 3-4). **D,** Schematic of the experimental design of the ADM formation assay using 3D

acinar cell explant system. **E,** Representative bright field images of acinar cell clusters and duct formation (ring structures) on day 5 of treatment with or without 50ng/mL TGF-α or 100nM insulin in the absence of trypsin inhibitor. ADM structures are indicated by red arrows. **F,** Quantification of the fold change in ADM events in primary mouse acinar cell 3D explants after 5 days of treatment with a combination of ± TGF-α and ± insulin and ± trypsin inhibitor. (n = 4 separate experiments, two-way ANOVA). Fold change values were calculated as treatment/negative control (no insulin or TGF-α or trypsin inhibitor) for each experiment. **G.** Schematic demonstrating obesity or diet-induced hyperinsulinemia, via Insr, promoted PanIN formation through increasing digestive enzymes production/release and its associated inflammation. Scale bars: 2 mm (A, B; top), 0.1 mm (A, B; bottom), and 100μm (E). Values are shown as mean ± SEM. *Adj. $p<0.05$, **Adj. $p<0.01$, ***Adj. $p<0.001$.

Figure S1. The *Ptf1a*^{CreER} allele labeled acinar cells and PanINs in 43.5-week-old mice.

A-B, Representative whole section (top) and high-magnification (bottom) images of immunohistochemical staining for GFP expressed from nTnG lineage tracing allele in 43.5-week-old male (**A**) and female (**B**) PK-*Insr*$^{w/w}$, PK-*Insr*$^{w/f}$, and PK-*Insr*$^{f/f}$ mice. **C-D**, Representative whole section (top) and high-magnification (bottom) images for immunohistochemical staining for GFP expressed from nTnG lineage tracing allele in 43.5-week-old male (**C**) and female (**D**) *Ptf1a*^{CreER}-*Insr*$^{w/w}$ and *Ptf1a*^{CreER}-*Insr*$^{f/f}$ mice. **E-F**, Representative whole section (top) and high-magnification (bottom) H&E images of pancreatic slides from 43.5-week-old male (**E**) and female (**F**) *Ptf1a*^{CreER}-*Insr*$^{w/w}$ and *Ptf1a*^{CreER}-*Insr*$^{f/f}$ mice. Scale bars: 2 mm (top) and 0.1mm (bottom).

Figure S2. Loss of *Insr* in acinar cells reduced ductal metaplasia and Alcian blue^{+} PanIN lesions.

A-B, Representative whole section (top) and high-magnification (bottom) images of immunohistochemical staining of Ck19 for male (**A**) and female (**B**) PK-*Insr*$^{w/w}$, PK-*Insr*$^{w/f}$, and PK-*Insr*$^{f/f}$ mice. **C-D,** Representative whole section (top) and high-magnification (bottom) images of pancreatic

939 slides from male (**C**) and female (**D**) PK-*Insr*$^{w/w}$, PK-*Insr*$^{w/f}$, and PK-*Insr*$^{f/f}$ mice stained with Alcian blue.
940 **E,** Quantification of Ck19^{+} area for mice from each genotype and sex (M or F) (n= 5-15). **F,**
941 Quantification of Alcian blue positive area for mice from each genotype and sex (M or F) (n= 5-16). **G-**
942 **H,** The correlation of acinar cell area and Ck19^{+} area for male (**G**) and female (**H**) mice. The maximum
943 value for Ck19^{+} area was ~20-30% due to stromal expansion in the parenchyma around the Ck19^{+}
944 area. Scale bars: 2 mm (top) and 0.1 mm (bottom). Values are shown as mean ± SEM. *p<0.05,
945 **p<0.01, ***p<0.001, ****p<0.0001.
946
947 **Figure S3. The *Ptf1a*^{CreER} allele labeled acinar cells and PanINs in 12-week-old mice.**
948 **A-B,** Representative whole section (top) and high-magnification (bottom) images of
949 immunohistochemical staining for GFP expressed from the nTnG lineage tracing allele in 12-week-old
950 male (**A**) and female (**B**) PK-*Insr*$^{w/w}$, PK-*Insr*$^{w/f}$, and PK-*Insr*$^{f/f}$ pancreata. Scale bars: 1mm (top) and 0.1
951 mm (bottom).
952
953 **Figure S4. *Kras*^{G12D} mutant mice had similar proteomics and phospho-proteomics changes as**
954 **human PDAC tumor samples.**
955 **A,** Plot of the top 20 mouse pathways from Reactome pathway enrichment for proteins that were
956 significantly up-or down-regulated (Adj. p<0.05) in PK-*Insr*$^{w/w}$ mice (n=3) compared to *Ptf1a*^{CreER}-
957 *Insr*$^{w/w}$ mice (n=3). The FDR for the same pathways from pathway enrichment with proteins from
958 human data that were significantly up- or down-regulated (Adj. p<10^{-19}) in normal (n=75)
959 compared to tumor samples (n=140) are also shown. The size of each dot represents the
960 proportion of genes inputted in all the genes found in each pathway. **B,** Plot of the top 20 mouse
961 pathways from Reactome pathway enrichment for proteins from corresponding phospho-sites that
962 were significantly up- or down-regulated (Adj. p<0.05) in PK-*Insr*$^{w/w}$ mice (n=3) compared to
963 *Ptf1a*^{CreER}-*Insr*$^{w/w}$ mice (n=3). The FDR for the same pathways from pathway enrichment with
964 proteins from corresponding phospho-sites from human data that were significantly up- or down-

965 regulated (Adj. $p<10^{-12}$) in normal (n=75) compared to tumor samples (n=140) are also shown.
966 The size of each dot represents the proportion of genes inputted in all the genes found in each
967 pathway.
968
969 **Figure S5. Loss of *Insr* in acinar cells reduced desmoplasia.**
970 **A-B,** The correlation of PanIN area and Sirius red^{+} area for male (**A**) and female (**B**) mice. *p<0.05.
971

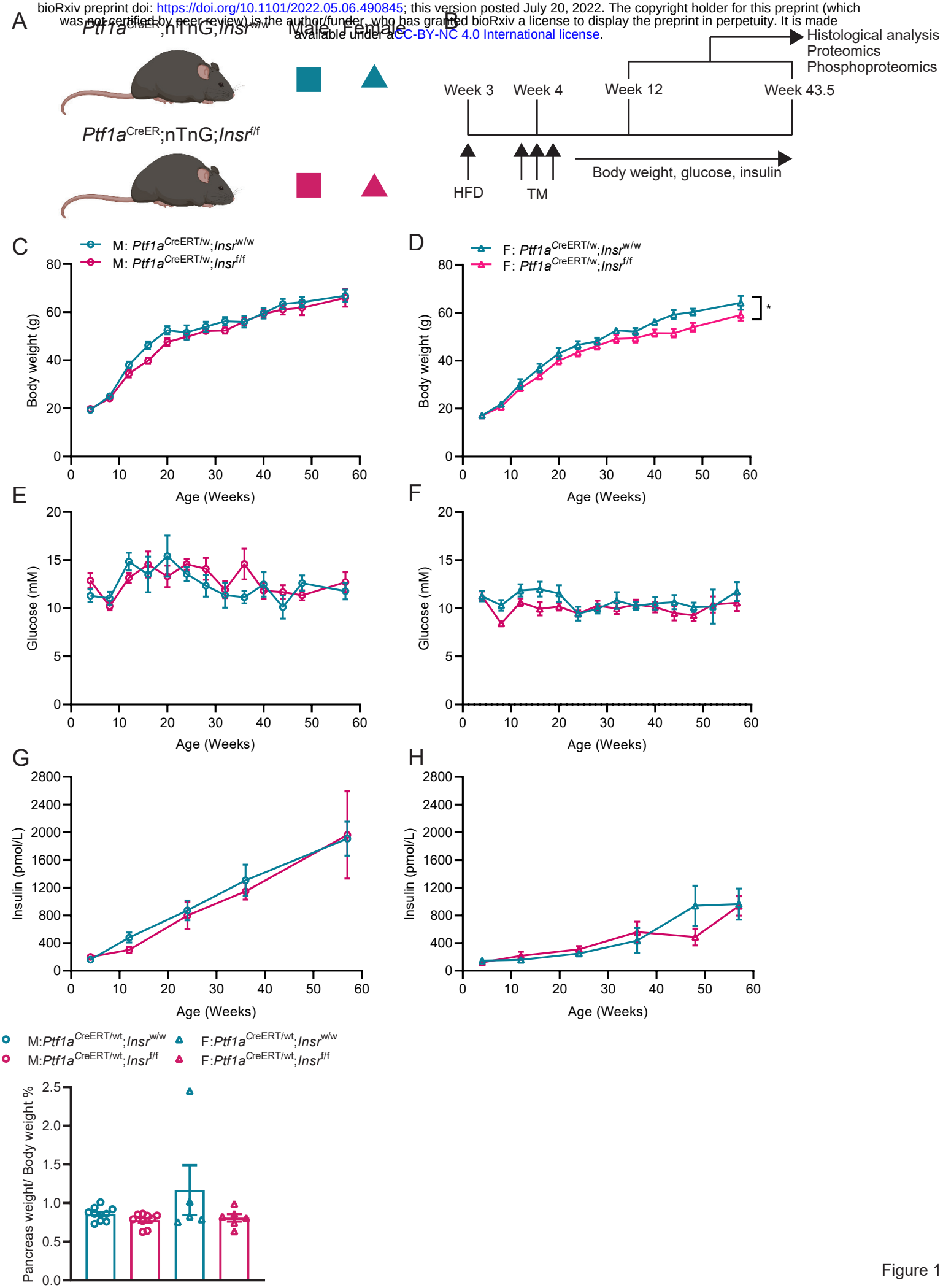

Figure 1

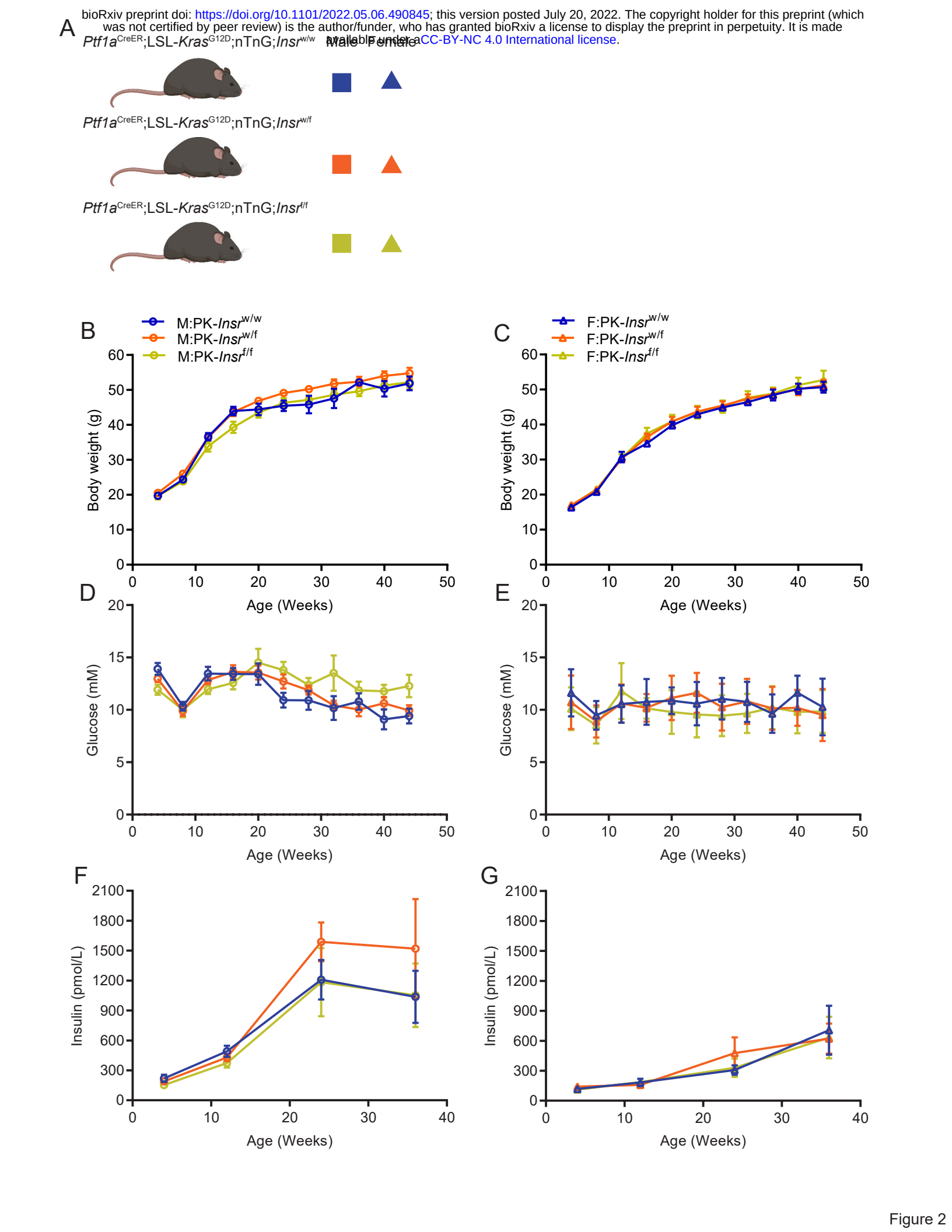

Figure 2

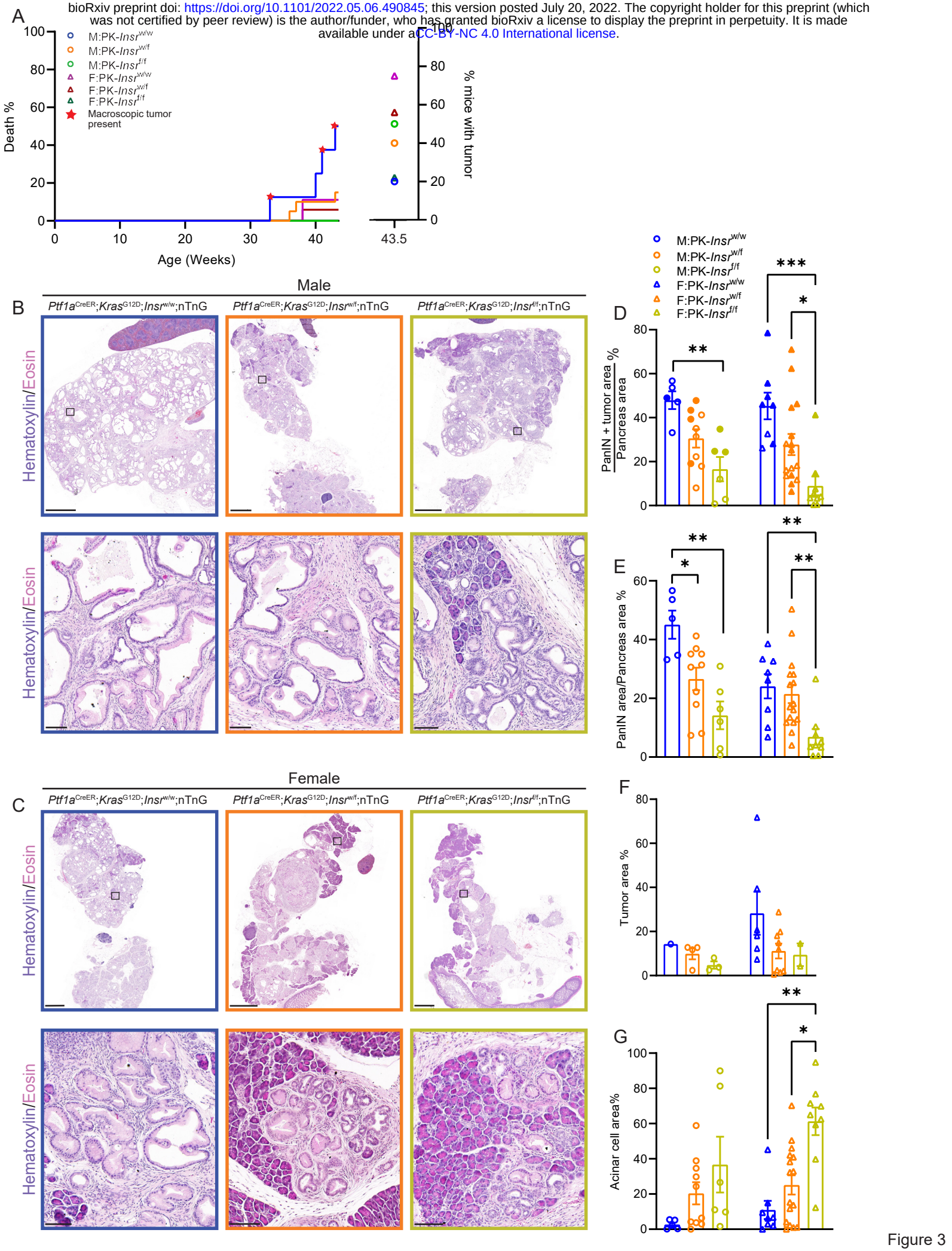

Figure 3

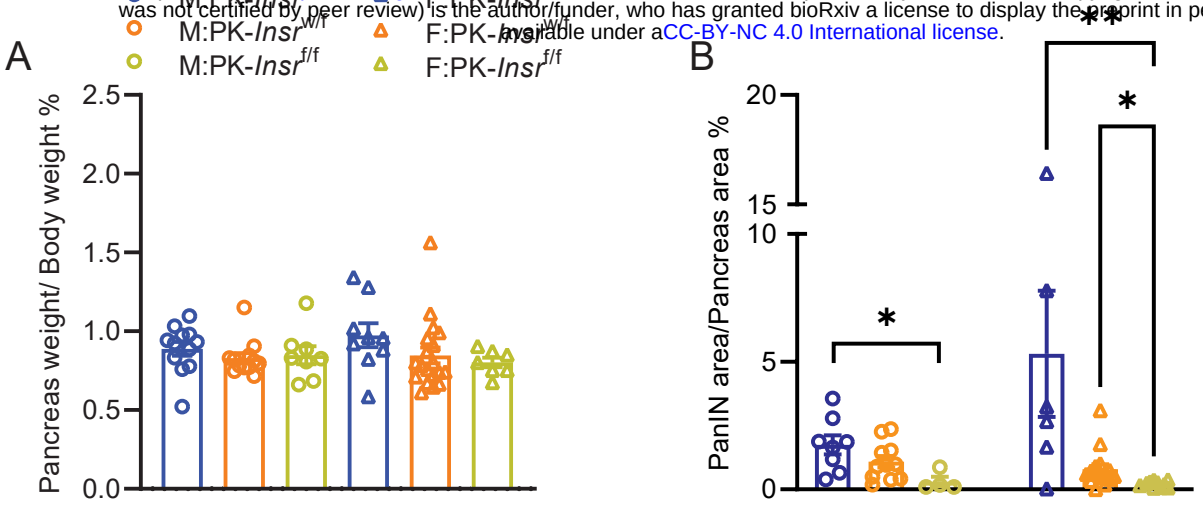

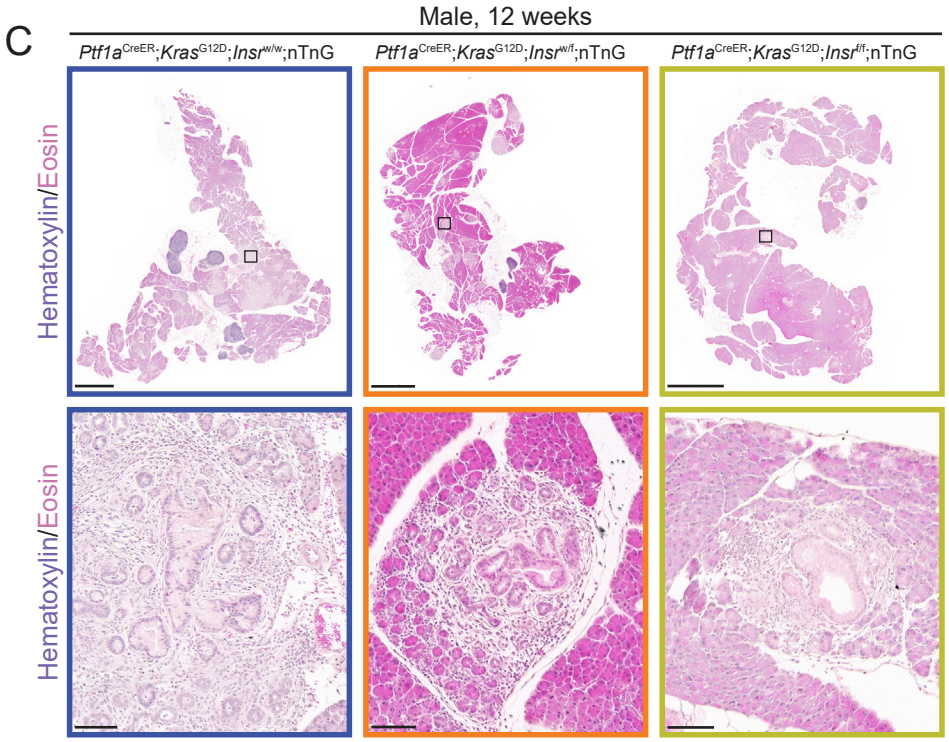

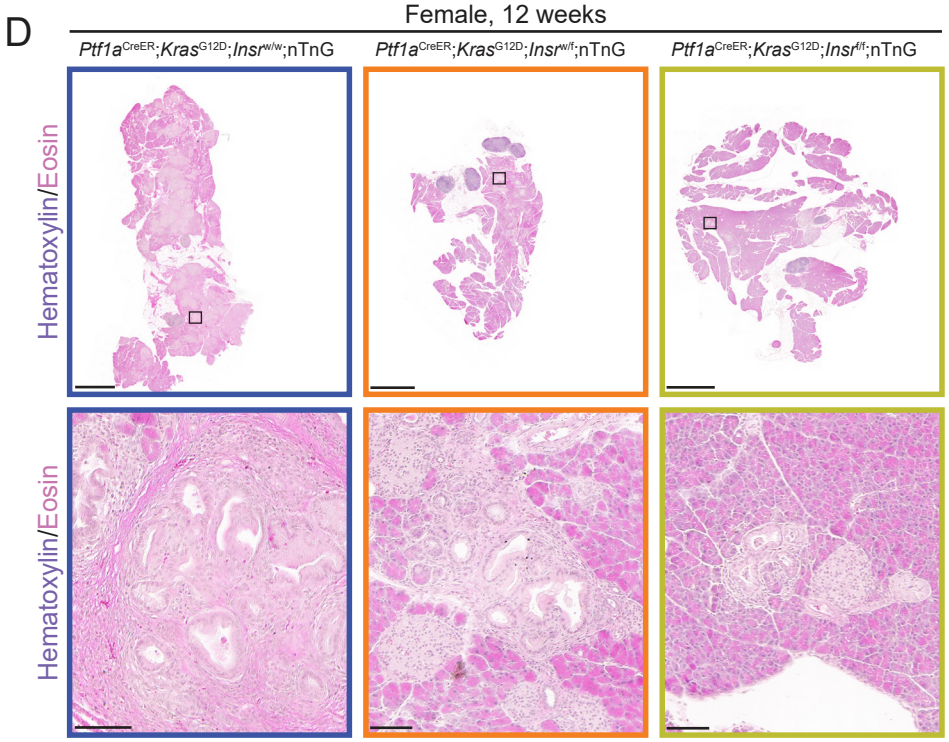

Figure 4

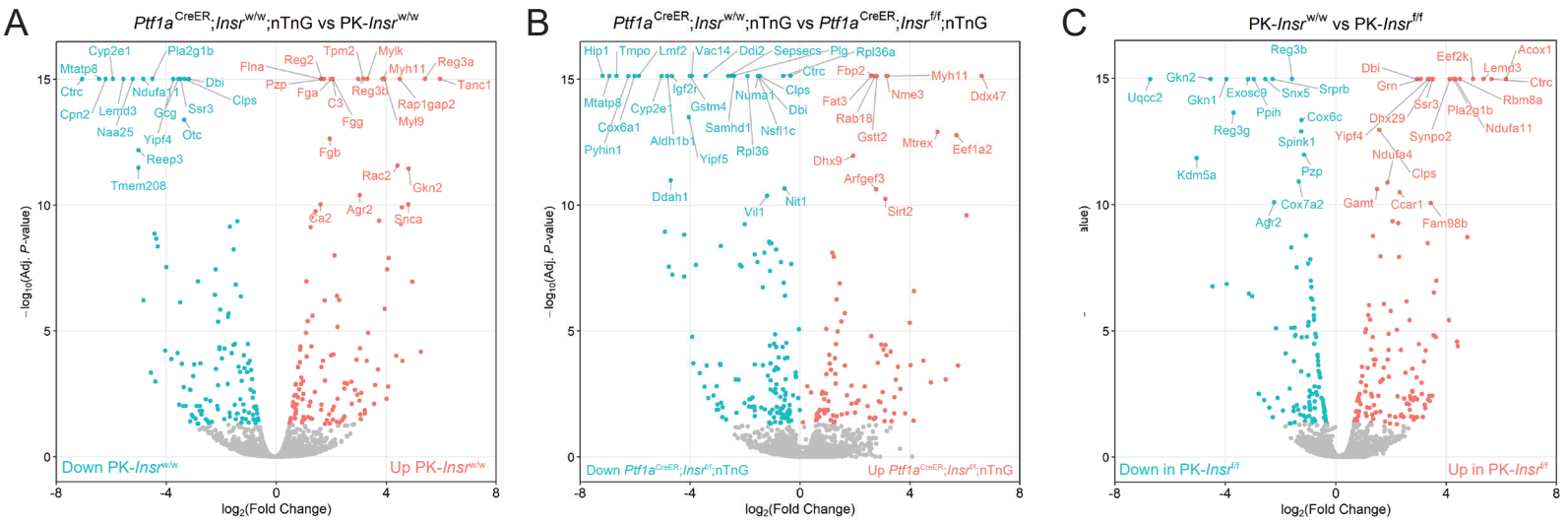

D

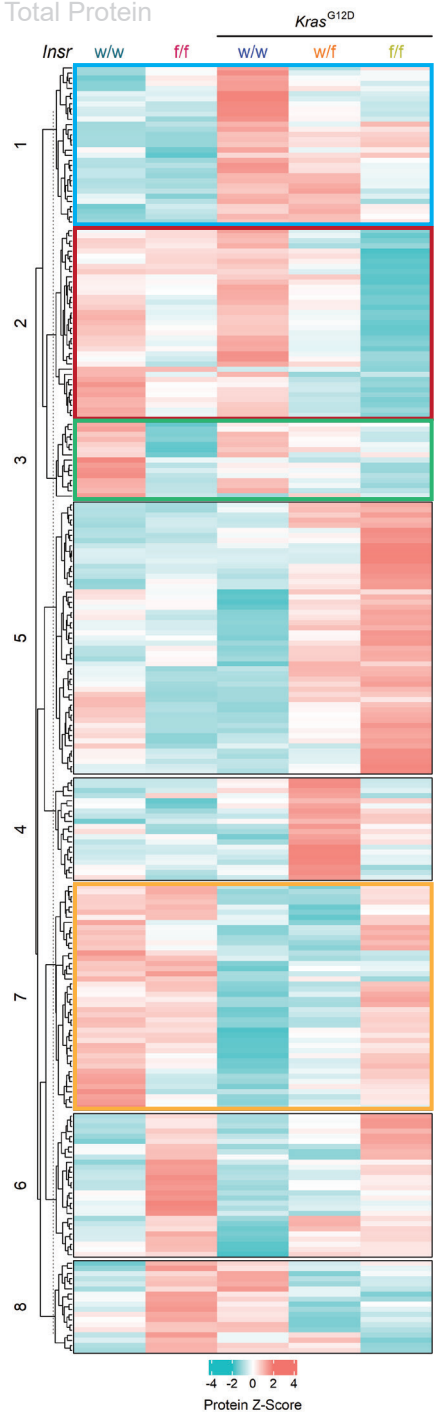

Cluster 1	Cluster 2	Cluster 3	Cluster 7
Clip1	Eif4ebp1	Atp5me	Ostc
Bag3	Snx5	Uqcr10	Cnbp
Ctss	Cel	Cox6c	Ilvbl
Rpl29	Ndufa7	Tbca	Gna14
Pzp	Cox7a2	Rpl36	Rap1b
Mzb1	Uqcc2	Plg	Mtnd3
Ppp4c	Emc10	Chchd4	Ssr3
Fis1	Sycn	Clps	Pla2g1b
Rbm26	Pnlip	Ube4a	Ubxn4
Actr1b	Ppih	Serf2	Nit1
Dmbt1	Pnliprp2	Igf2r	Srp68
Tmsb10	Acly	Tmc4	Rap1a
Reg2	Trmt112	Amy1	Eef2k
Fgg	Ctrb1	Kdm5a	Dctn3
Fga	Pcna	Tmem41a	Cbs
Fgb	Uqcrq		Tmem97
Sh3bgrl3	Afdn		Ctrc
Pxn	Cela3b		Gcg
Reg3a	Tcea1		Stap2
Reg3b	Cpa1		Adh5
Apoa2	Cpa2		Rps24
S100a6	Klk1		Bzw1
Igh-3	Spink1		Wdr77
Tf	Pnliprp1		Tpk1
Gkn1	Prss2		Nploc4
Tmem43	Cox17		Ube2g2
Pklr	Sra1		Aifm1
Tagln	Uqcrh		Lemd3
Mt1	Dhcr7		Yipf4
Hpx	Srprb		Ndufa11
FAM120A	Galnt6		Lonp1
	Cela1		mt-Co3
	Cela2a		Snrnp200
	Alcam		Mtnd4
	Amy2		Iah1
	Cuzd1		Hm13
	Rnase1		Nfasc
			Ca3
			Fabp4
			Srsf5
			Creb1
			Ap1s1
			Use1
			Krt1

Figure 5

A

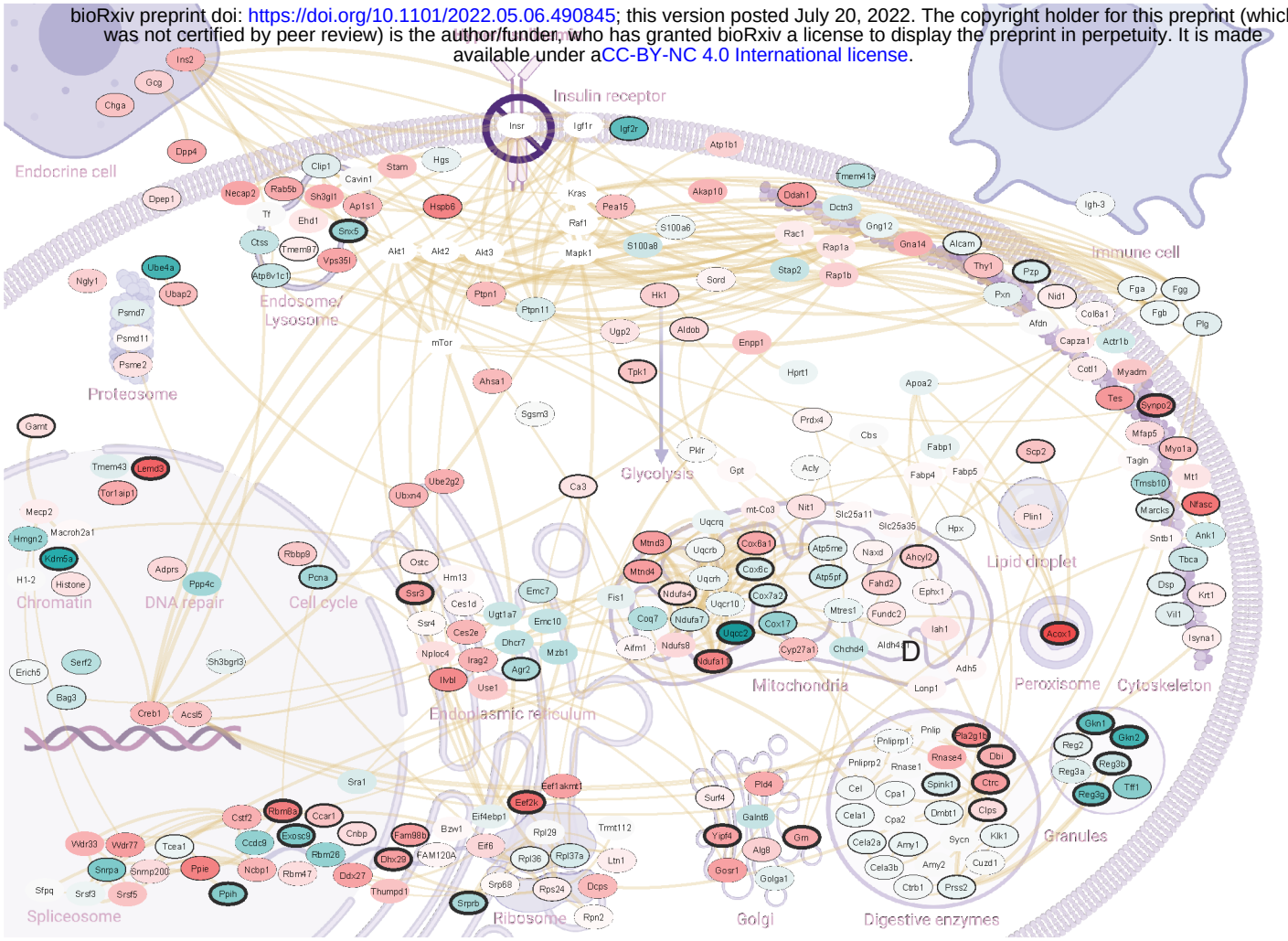

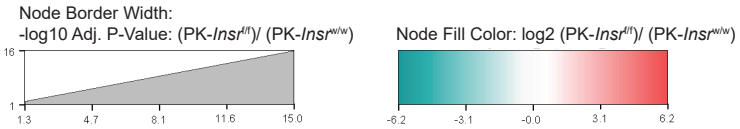

B

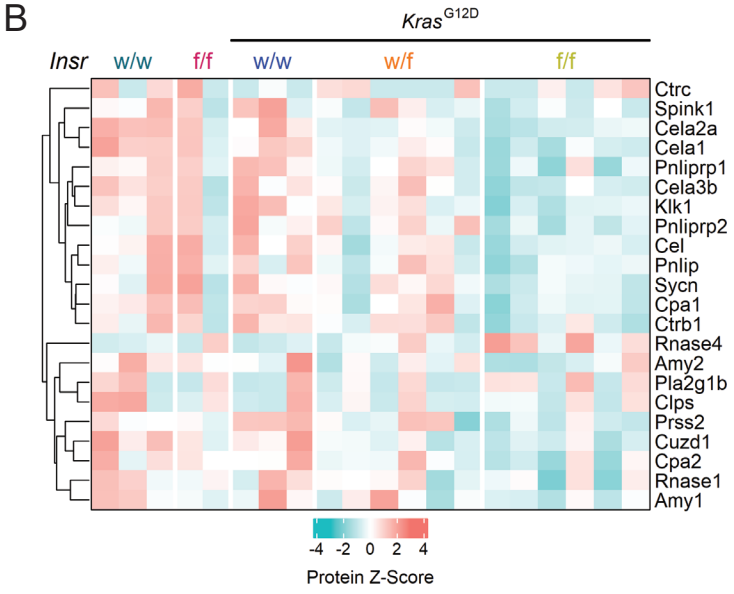

C

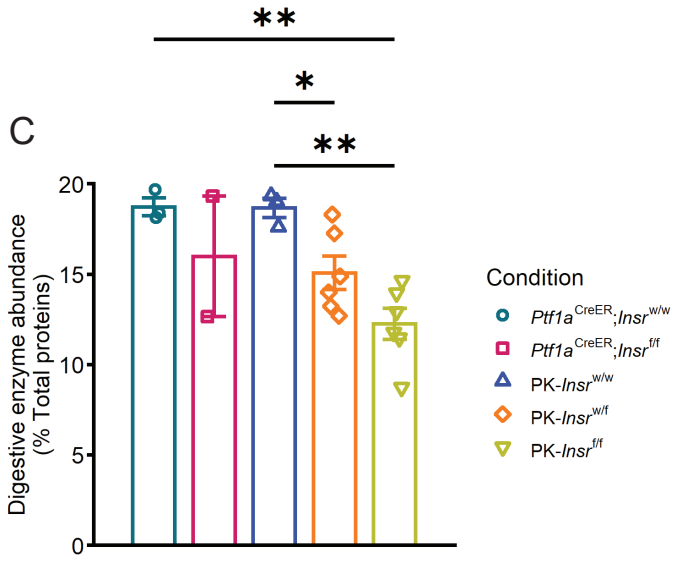

Figure 6

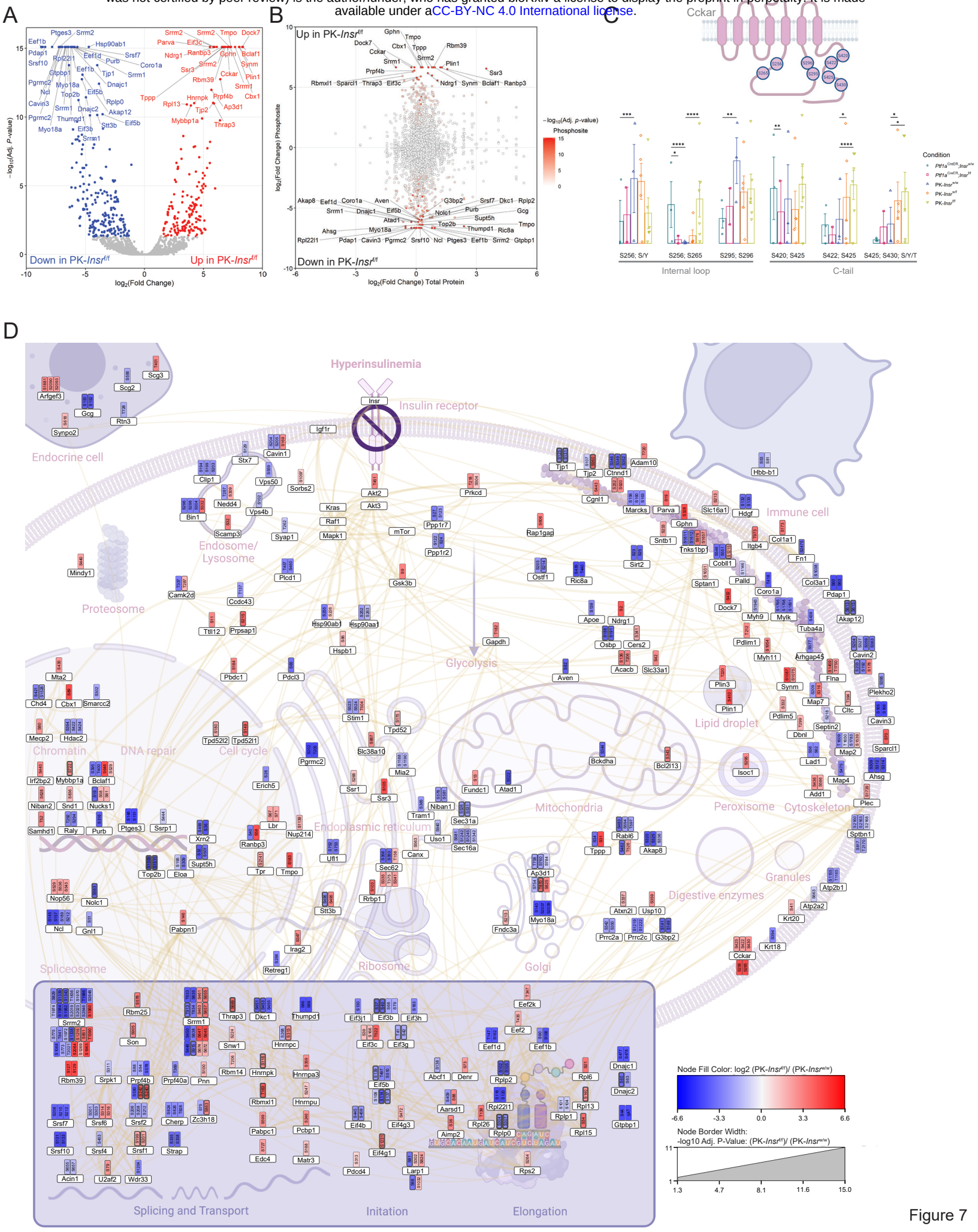

Figure 7

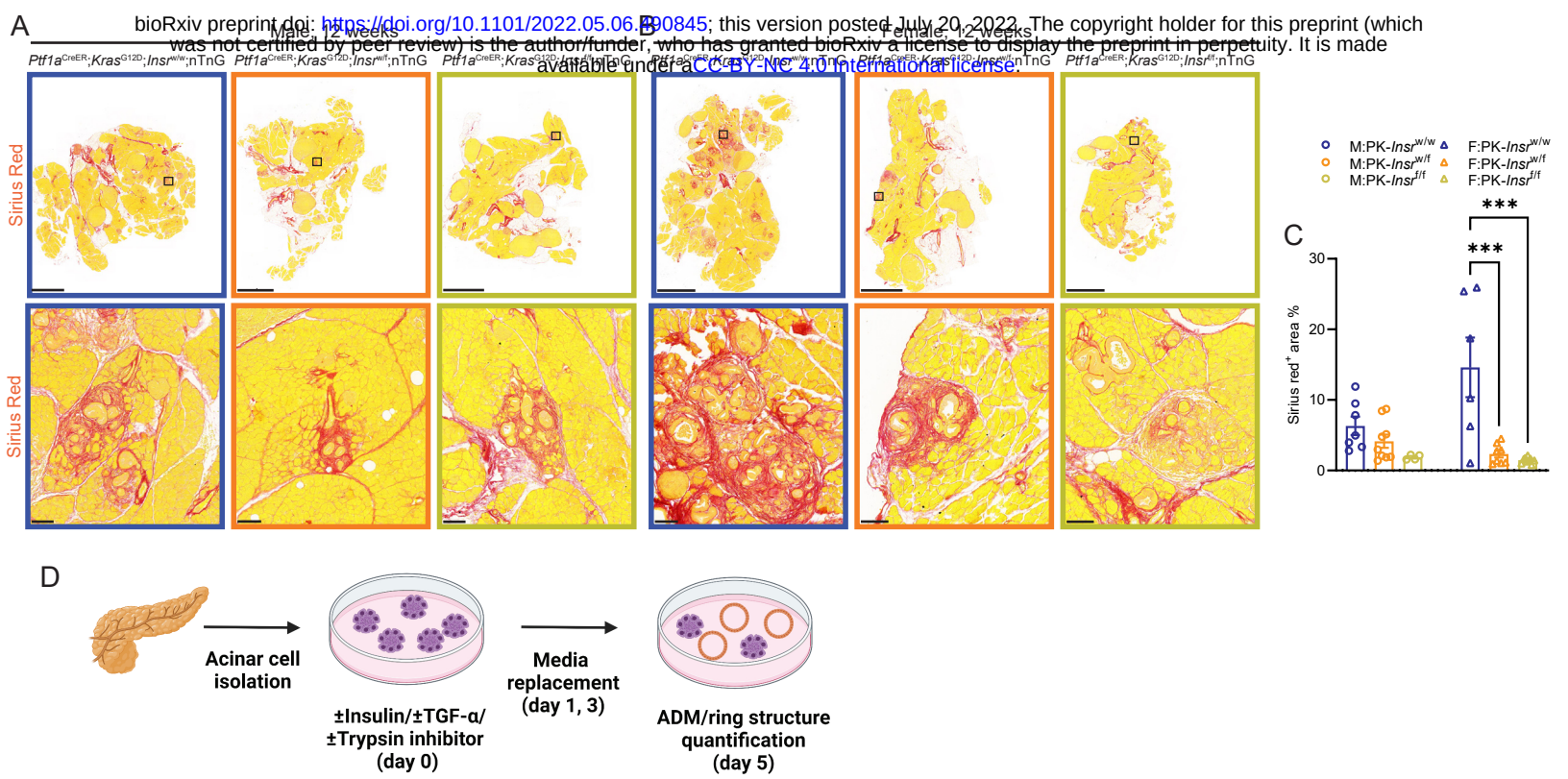

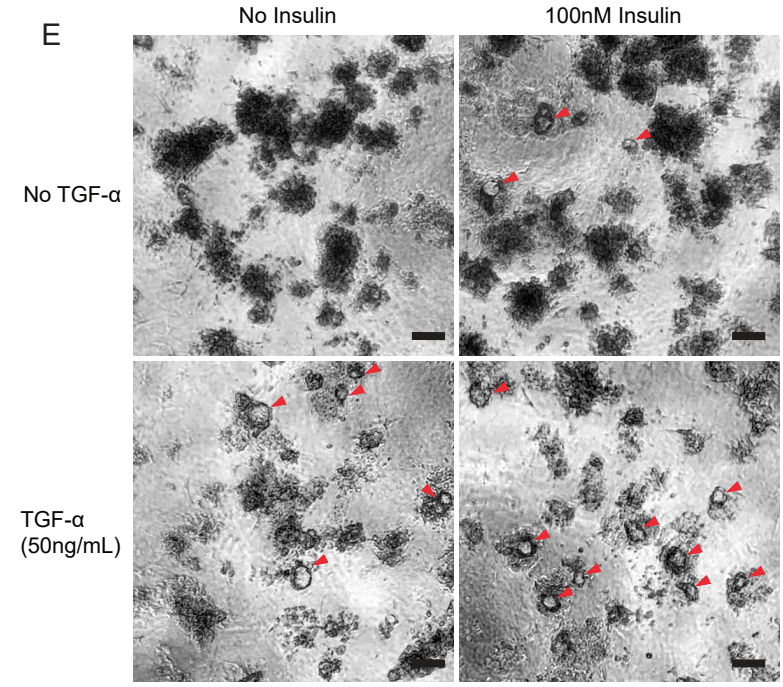

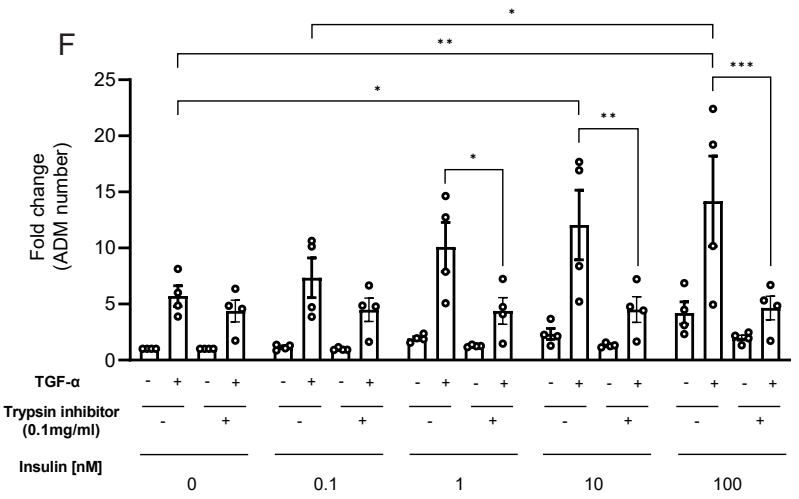

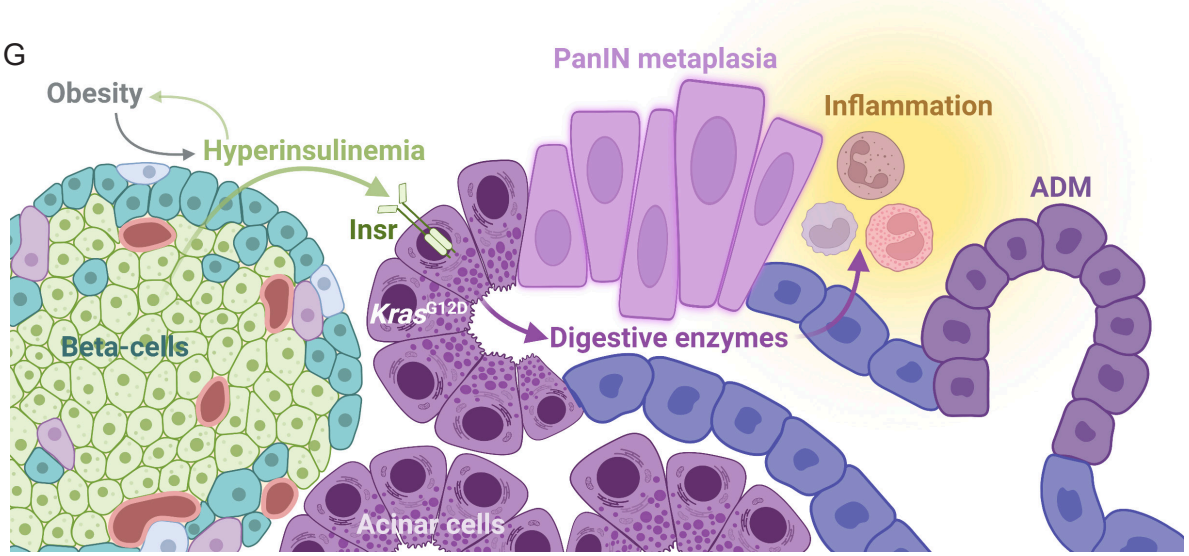

Figure 8

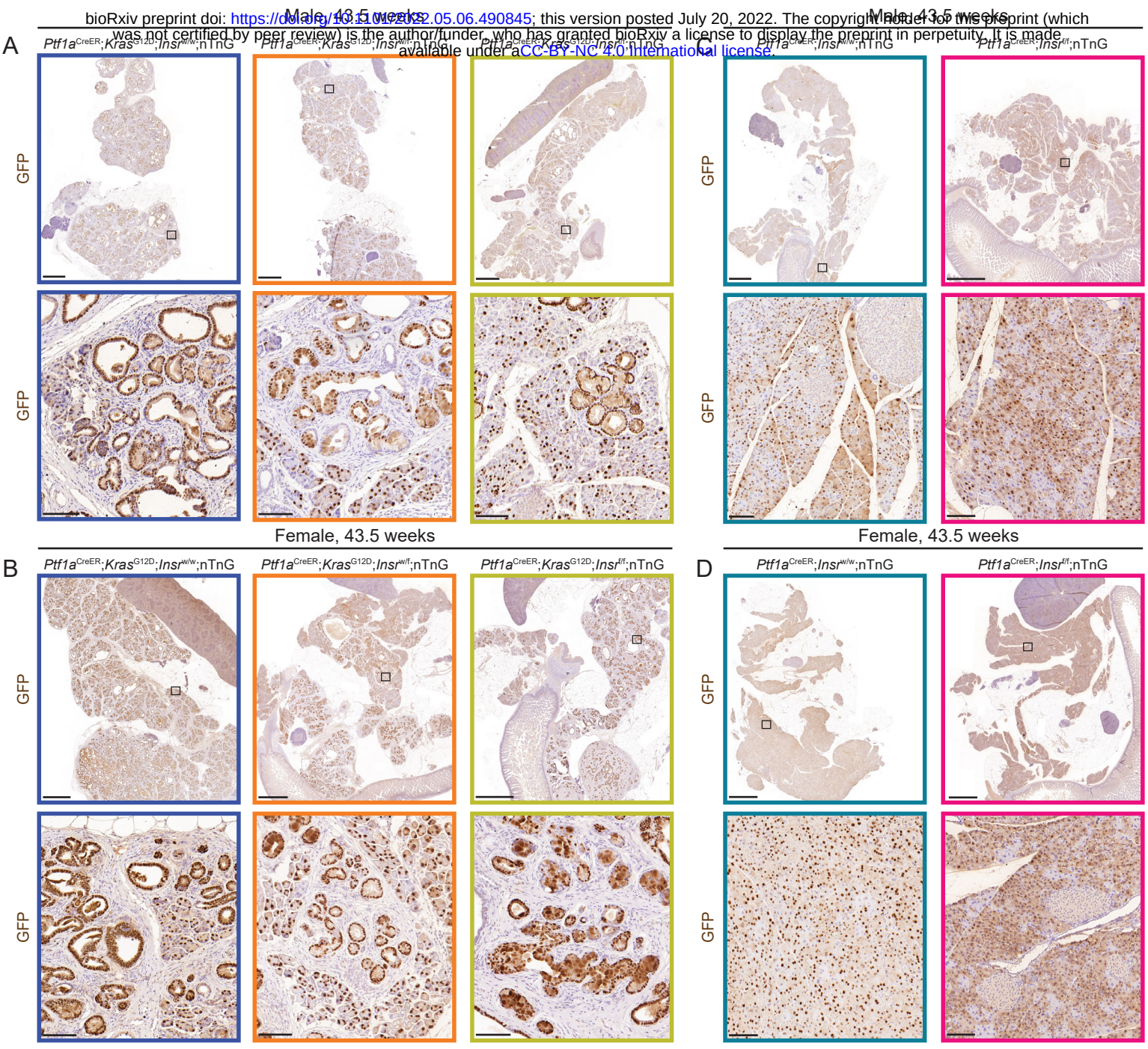

Figure S1

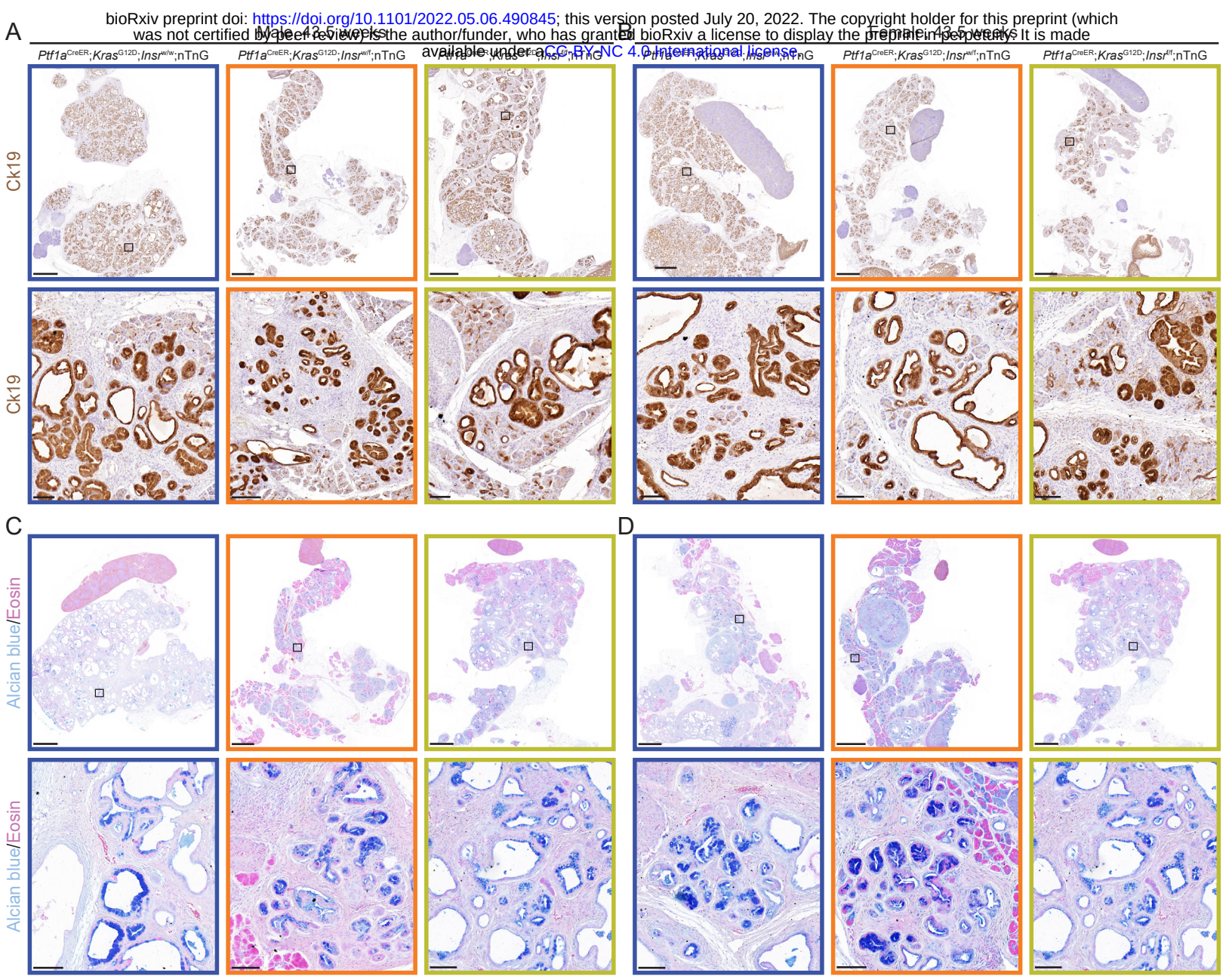

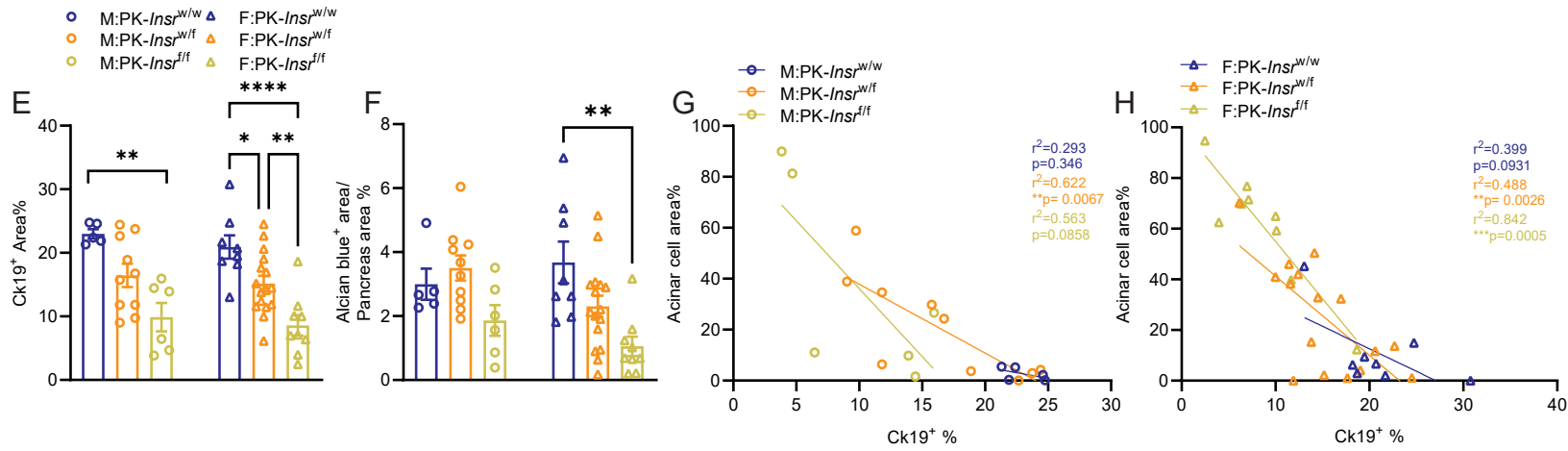

Figure S2

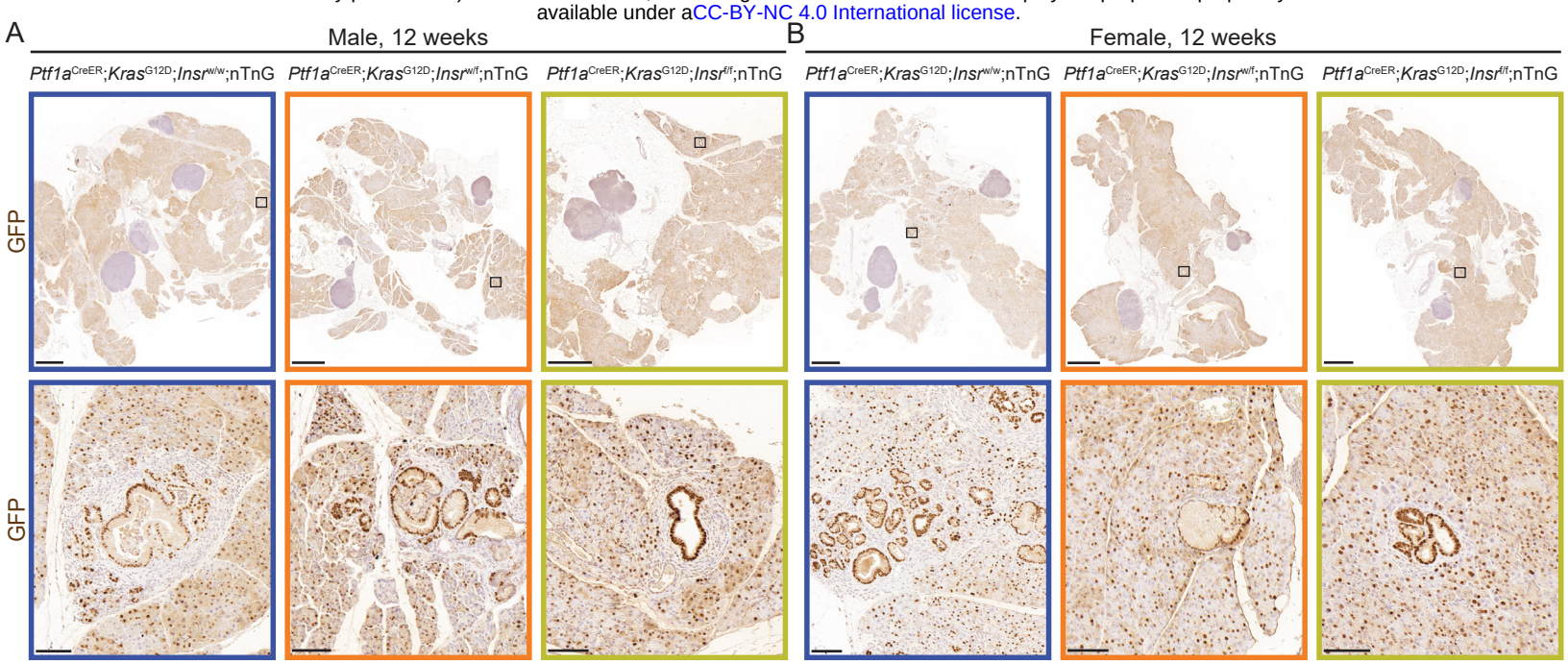

Figure S3

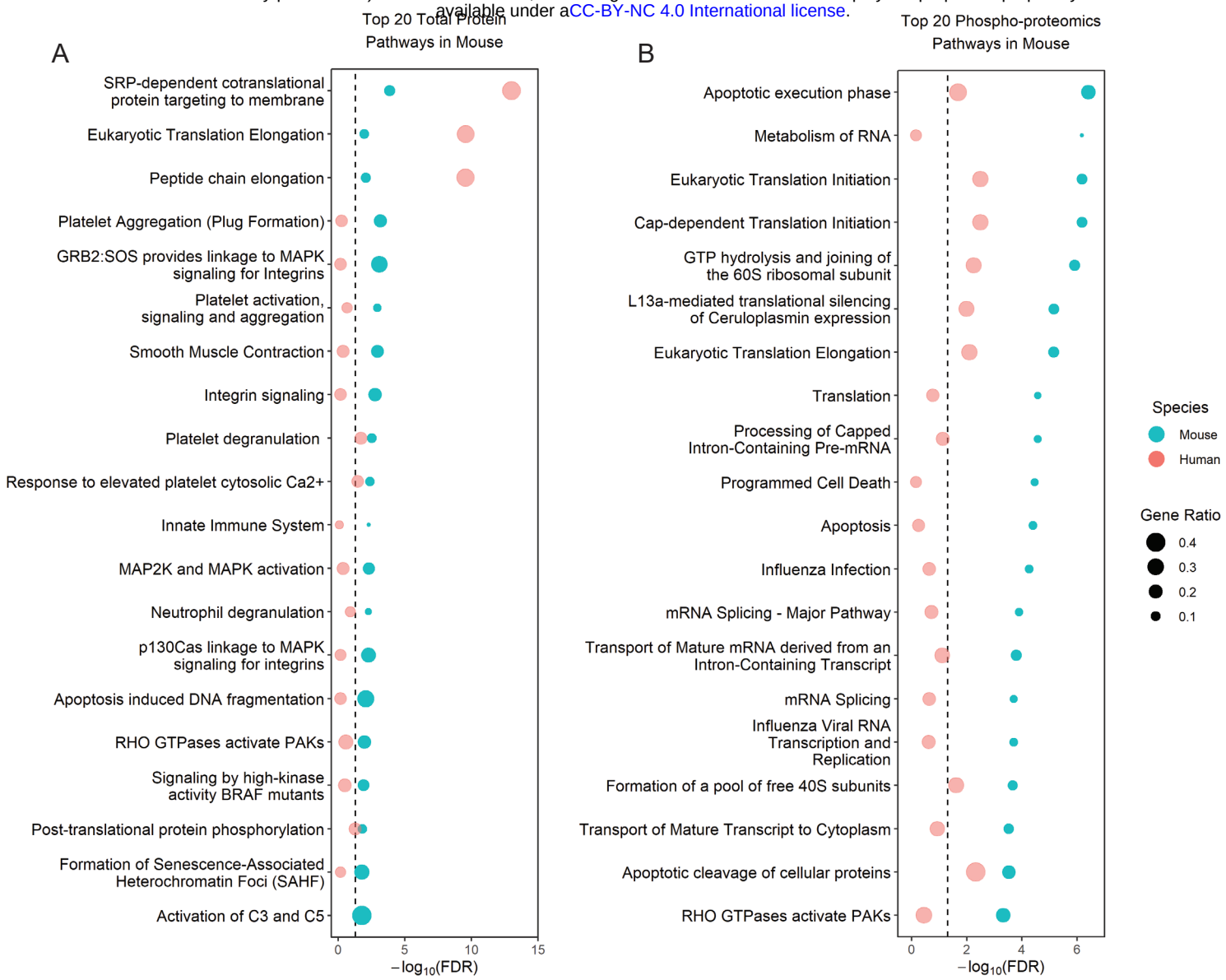

Figure S4

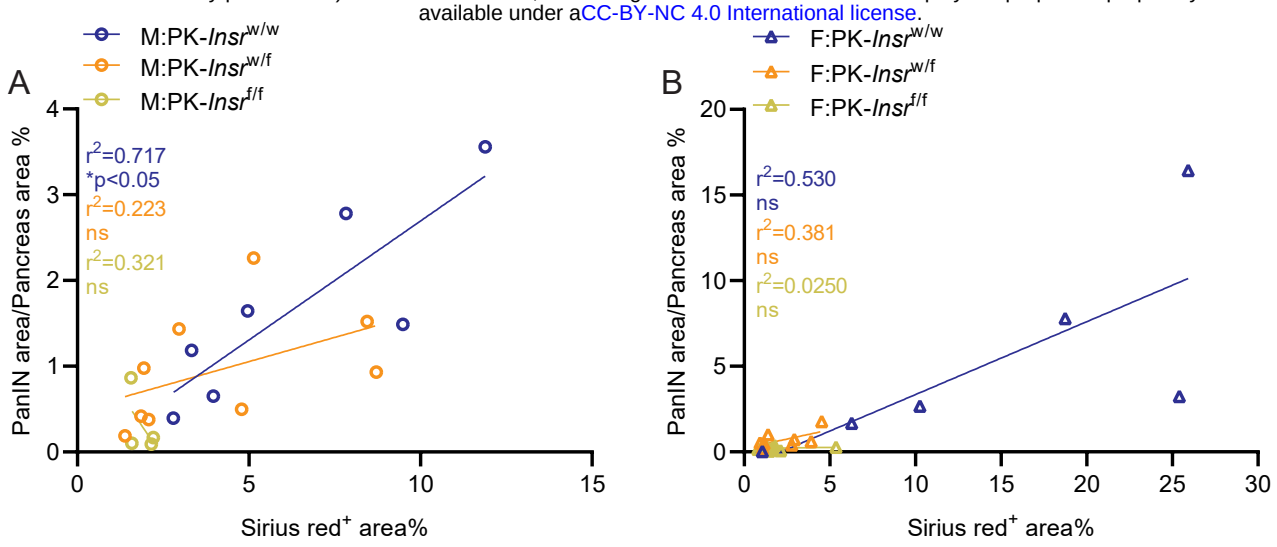

Figure S5